MAP7 family proteins are microtubule-tethered allosteric activators of kinesin-1

Peter Jan Hooikaas[1*], Maud Martin[1*], Gert-Jan Kuijntjes[1], Cathelijn A.E. Peeters[1], Eugene A. Katrukha[1], Luca Ferrari[2], Riccardo Stucchi[1], Daan G.F. Verhagen[1], Wilhelmina E. van Riel[1], A.F. Maarten Altelaar[3], Casper C. Hoogenraad[1], Stefan G.D. Rüdiger[2], Lukas C. Kapitein[1] and Anna Akhmanova[1] #

[1] Cell Biology, Department of Biology, Faculty of Science, Utrecht University, Padualaan 8, 3584 CH Utrecht, the Netherlands

[2] Cellular Protein Chemistry, Bijvoet Center for Biomolecular Research, Utrecht University, Padualaan 8, 3584 CH Utrecht, The Netherlands.

[3] Biomolecular Mass Spectrometry and Proteomics, Bijvoet Center for Biomolecular Research, Utrecht Institute for Pharmaceutical Sciences and The Netherlands Proteomics Centre, Utrecht University, Padualaan 8, 3584 CH Utrecht, The Netherlands.

* These authors contributed equally

Condensed title: **Regulation of Kinesin-1 by MAP7 family proteins**

Corresponding author: Anna Akhmanova, a.akhmanova@uu.nl

Abstract

Kinesin-1 is responsible for microtubule-based transport of numerous cellular cargoes. Here, we explored the regulation of kinesin-1 by MAP7/ensconsin family proteins. We found that all four mammalian MAP7 family members bound to kinesin-1, and MAP7, MAP7D1 and MAP7D3 acted redundantly to enable kinesin-1-dependent transport in HeLa cells. Microtubule recruitment of the truncated kinesin-1 KIF5B-560, which contains the stalk but not the cargo-binding and autoregulatory regions, was inhibited in cells co-depleted of these three MAP7 proteins. In vitro, purified MAP7 and MAP7D3 increased microtubule landing rate and processivity of KIF5B-560. The same was true for MAP7D3 C-terminus, which weakly bound to microtubules and exchanged rapidly on motile KIF5B-560 motors. A C-terminal MAP7 fragment lacking microtubule affinity increased KIF5B-560 recruitment to microtubules in vitro and in cells, and partially rescued kinesin-1-dependent transport in the absence of full-length MAP7 proteins. We propose that MAP7 proteins are microtubule-tethered kinesin-1 activators, with which the motor transiently interacts as it moves along microtubules.

Summary

A combination of experiments in cells and in vitro reconstitution assays demonstrated that mammalian MAP7 family proteins act redundantly to activate kinesin-1 and promote its microtubule binding and processivity by transiently associating with the stalk region of the motor.

Introduction

Kinesins are molecular motors responsible for the transport of different organelles and macromolecular complexes along microtubules (MTs) and for controlling MT organization and dynamics (Hirokawa and Tanaka, 2015; Verhey et al., 2011). The spatial and temporal control of kinesin localization and activity depends on numerous factors, such as cargo adaptors and post-translational modifications of both motor complexes and MTs (Akhmanova and Hammer, 2010; Fu and Holzbaur, 2014; Verhey and Hammond, 2009). In addition, MT-associated proteins (MAPs) that decorate MT tracks can affect kinesin recruitment and behavior. For example, during cell division, a MT-bundling protein PRC1 recruits kinesin-4 to antiparallel MTs within the spindle midzone to control MT length (Bieling et al., 2010; Subramanian et al., 2013). Kinesin-3 dependent membrane transport in neurons is regulated by the MAPs doublecortin and doublecortin-like kinase 1, which promote motor binding to MTs (Lipka et al., 2016; Liu et al., 2012), and MAP4 serves as a positive regulator of kinesin-2-mediated dispersion of pigment granules in frog melanophores (Semenova et al., 2014).

Kinesin-1 is the major MT plus-end directed motor involved in a broad variety of transport processes (Akhmanova and Hammer, 2010; Hirokawa and Tanaka, 2015; Verhey et al., 2011). This motor is well known to be regulated by different MAPs. Neuronal MAPs tau and MAP2 inhibit kinesin-1-driven motility (Dixit et al., 2008; Ebneth et al., 1998; Gumy et al., 2017; Monroy et al., 2018; Seitz et al., 2002; Trinczek et al., 1999; Vershinin et al., 2007). In contrast, MAP7 family members are firmly established to be positive regulators of kinesin-1 (Barlan et al., 2013; Metivier et al., 2018; Metzger et al., 2012; Monroy et al., 2018; Sung et al., 2008). MAP7 proteins are represented by a single homologue, ensconsin, in flies and by four isoforms encoded by different genes, MAP7, MAP7D1, MAP7D2 and MAP7D3, in mammals (Bulinski and Bossler, 1994; Metzger et al., 2012; Yadav et al., 2014). All MAP7 family members have a similar organization, with two conserved domains that are predicted to be helical, interspersed with unstructured regions. The N-terminal domain of MAP7 proteins strongly interacts with MTs, while the C-terminal domain binds to the stalk region of kinesin-1 (Metzger et al., 2012; Monroy et al., 2018; Sun et al., 2011)(Fig. 1A). The C-terminal region of MAP7D3 was also shown to have a weak MT affinity (Yadav et al., 2014). In flies, it was demonstrated that ensconsin is an essential kinesin-1 cofactor, required for numerous processes such as transport of

mitochondria, peroxisomes, ribonucleoprotein particles, MT sliding, cytoplasmic flow in oocytes, neuronal development, centrosome separation and nuclear positioning in muscle cells (Barlan et al., 2013; Metivier et al., 2018; Metzger et al., 2012; Monroy et al., 2018; Sung et al., 2008). Also in mammalian myotubes, MAP7 is needed for proper kinesin-1-dependent nuclear distribution (Metzger et al., 2012), but whether this applies to other cell types and kinesin-1-dependent processes in mammals has not been investigated. It is also unknown whether mammalian MAP7 homologues all behave similarly and whether they show different, overlapping or redundant functions.

There are also important unresolved questions concerning the mechanism of cooperation between kinesin-1 and MAP7. In vitro experiments in fly ovary extracts have shown that the minimal dimeric kinesin-1 fragment does not require ensconsin, but the full-length kinesin-1 is no longer able to productively interact with MTs in the absence of ensconsin (Sung et al., 2008). Recent in vitro reconstitution work with purified proteins demonstrated that MAP7 recruited kinesin-1 to MTs and somewhat decreased motor velocity but had only a mild effect on kinesin-1 run length (Monroy et al., 2018). Importantly, MAP7 was highly immobile in these assays and was not co-transported with the motor, suggesting that MAP7 affects only the initial recruitment of the kinesin to MTs but has little impact on kinesin-1 movement (Monroy et al., 2018). However, some observations in flies do not agree with this simple model, as it was shown that the C-terminal fragment of ensconsin, which lacks the MT-binding domain (Sung et al., 2008), significantly rescues kinesin-1-related transport deficiencies in cells lacking ensconsin (Barlan et al., 2013; Metivier et al., 2018). Kinesin-1 is well known to be autoinhibited by its C-terminal cargo-binding domains (Verhey and Hammond, 2009), and it was proposed that ensconsin plays a role in relieving autoinhibition of the kinesin (Barlan et al., 2013). This possibility could be in line with the experiments performed in extracts (Sung et al., 2008), but it was not yet tested with purified proteins.

Here, we explored the relationship between kinesin-1 activity and mammalian MAP7 proteins. We found that all four mammalian MAP7 family members are able to bind kinesin-1. Three of these proteins, MAP7, MAP7D1 and MAP7D3, are expressed in HeLa cells (Kikuchi et al., 2018; Syred et al., 2013), and only co-depletion of all three MAP7's but not their individual loss affected kinesin-1-dependent distribution of mitochondria. Interestingly, in cells lacking these

three MAP7 homologues, a fragment of kinesin-1, KIF5B-560 (Case et al., 1997), which contains the motor domain and the dimerizing stalk with the MAP7-binding site, but not the cargo-binding and autoinhibitory domains, lost its MT association. This result was surprising, because this kinesin-1 fragment is thought to be constitutively active. MT recruitment of KIF5B-560 was rescued not only by full-length MAP7s, but also by their C-terminal domains, which lacked the major MT-binding region. These results were recapitulated in in vitro reconstitution assays with purified proteins, including the C-terminus of MAP7D3, which weakly binds to MTs, and the C-terminus of MAP7, which displays no MT binding. The kinesin-binding region of MAP7 can thus activate the motor, possibly by allosterically stabilizing a conformation favorable for MT interaction.

In agreement with published data, we found that MAP7 was immobile on MTs in vitro (Monroy et al., 2018). In contrast, MAP7D3 interacted with MTs less tightly, and could be observed moving together with KIF5B-560 motors. In spite of these differences, both MAPs increased not only the recruitment of kinesin-1 to MT but also its processivity. Such an effect can only be explained if the interaction between MAP7s and kinesin-1 is transient. This was indeed confirmed by showing that MAP7D3 C-terminus rapidly exchanges on motile KIF5B-560 motors. Taken together, our data show that MAP7 proteins redundantly regulate kinesin-1-dependent transport by acting as MT-tethered activators of this kinesin.

Results

MAP7 family members act redundantly in mitochondrial distribution in HeLa cells

To test whether all four MAP7 family members can potentially act as kinesin-1 regulators, we performed a pull down assay with individual tagged MAP7 proteins and KIF5B-560 and found that all four MAP7 homologues could indeed bind to this kinesin-1 deletion mutant (Fig. 1A, B). Gene expression analysis at the mRNA and protein level indicated that HeLa cells co-express MAP7, MAP7D1 and MAP7D3 (Kikuchi et al., 2018; Syred et al., 2013), and we confirmed these data by antibody staining (Fig. 1C). In contrast, MAP7D2, which is highly expressed in brain tissue (Niida and Yachie, 2011), was not expressed in HeLa cells. To test if all three MAP7's are required for kinesin-1 function, we initially used the distribution of mitochondria as readout, because, as published previously, it strongly depends on kinesin-1 KIF5B (Tanaka et al., 1998). In the absence of KIF5B, mitochondria were no longer dispersed in the cytoplasm but were instead clustered around the nucleus (Fig. 1D, G, H). Next, we generated HeLa cells lacking each individual MAP7 family member, but observed no defects in the localization of mitochondria (Fig. 1E-H). In addition, no compensatory effects were found within the MAP7 family when one of the MAPs was depleted (Fig. 1E, F).

We next attempted to generate a stable triple knockout of MAP7, MAP7D1 and MAP7D3, but such cells were not viable. This was unlikely due to the lack of kinesin-1-mediated transport, as KIF5B knockout cells displayed no apparent growth or proliferation defects, and the two other kinesin-1 isoforms, KIF5A and KIF5C, do not seem to be expressed in HeLa cells (Nagaraj et al., 2011). Although MAP7 was shown to be phosphorylated and thus inactivated during mitosis (McHedlishvili et al., 2018), it is possible that MAP7 proteins still contribute to cell division, as ensconsin is known to participate in spindle formation in flies (Gallaud et al., 2014), and MAP7D3 was reported to modulate the recruitment of kinesin-13 to the mitotic spindle (Kwon et al., 2016). In order to remove all three MAP7 homologues simultaneously, we performed siRNA-mediated knockdown of MAP7D1 and MAP7D3 in the stable MAP7 knockout line, and this approach resulted in an efficient loss of all three MAP7 family members (Fig. 1F). Depletion of all three MAP7 homologs mimicked the effect of KIF5B knockout, leading to a strong perinuclear accumulation of mitochondria (Fig. 1I, J). This defect was rescued by re-expressing in these cells the individual full length MAP7 proteins (Fig. 1J). Furthermore, mitochondrial

distribution was partially rescued by expressing the C-termini of MAP7 and MAP7D1 (Fig. 1J). Rescue with the MAP7D3 C-terminus was less efficient, because the construct was mostly accumulated in the nucleus, and, as its concentration in the cytoplasm was low, only highly expressing cells showed rescue (Fig. S1A). Importantly, we observed no enrichment of MAP7 C-termini along MTs (Fig. S1B, mCherry channel). In contrast, the N-terminal domains of all three MAP7 proteins nicely labeled the MT network but completely failed to rescue the distribution of mitochondria in cells lacking all endogenous MAP7s (Fig. 1J and S1B). We conclude that MAP7 family members act redundantly in KIF5B-dependent mitochondria localization, and that their C-termini, which display no or only low affinity for MTs, are sufficient to support this function.

KIF5B-560 binding to MTs in cells depends on MAP7 proteins

To show that the loss of MAP7 proteins has a direct effect on kinesin-1 activity, we next examined the distribution of the dimeric KIF5B-560 truncation mutant that can move along MTs but does not bind to cargo. In control HeLa cells, this construct was distributed along MTs, and in most cells, it showed enhanced accumulation on MTs in cell corners, where MT plus ends are concentrated (Fig. 2A). Depletion of individual MAP7 family members did not alter this distribution except for the knockout of MAP7D3, in which less KIF5B-560 accumulated at corner MTs (Fig. 2A, B). In contrast, in cells lacking all three MAP7 proteins, KIF5B-560 showed a diffuse localization (Fig. 2C). Expression of MAP7, MAP7D1 or MAP7D2 in such cells rescued the recruitment of the kinesin to MTs, whereas expression of MAP7D3 led to strong co-accumulation of both constructs in the corners of all transfected cells (Fig. 2D-F). Expression of the N-terminal, MT-binding fragments of MAP7 and its homologs could not restore the distribution of KIF5B-560, while significant rescue of MT binding by the kinesin was observed with the C-termini of MAP7 and MAP7D1 (Fig. 2E and S1B). We conclude that KIF5B-560 has low affinity for cellular MTs in the absence of MAP7, and that this affinity can be increased by diffusely localized kinesin-1-binding MAP7 fragments. The C-terminus of MAP7D3, which was mostly nuclear on its own (Fig. S1A), was retained in the cytoplasm when expressed together with KIF5B-560, and shifted the localization of this kinesin fragment to MTs in cell corners, similar to the full-length MAP7D3 (Fig. 2D, E and S1B).

MAP7D3 but not MAP7 can be redistributed by kinesin-1

To understand why MAP7D3 but not the other MAP7 homologues promotes MT plus-end shifted distribution of KIF5B-560, we next examined the distribution of the endogenous MAP7 and MAP7D3 and found that only MAP7D3 could be efficiently relocalized by KIF5B-560 to cell corners (Fig. 3A, B).

To prove that kinesin-1 can indeed rapidly relocalize MAP7D3, we have set up an optogenetics-based assay, in which KIF5B-560 could be sequestered in the nucleus and then acutely released from it using a blue light-inducible nuclear export system (Niopek et al., 2016). A KIF5B-560-mCherry, containing NLS sequences, was C-terminally tagged with an engineered domain of *Avena sativa* phototropin-1, AsLOV2, in which the Jα helix was modified to contain a nuclear export signal. Within 1 to 2 minutes after activation with blue light, KIF5B-560 was efficiently exported from the nucleus (Fig. 3D, E, G, H). MAP7D3, but not MAP7 co-accumulated on MTs in cell corners within a 4-minute timeframe (Fig. 3D-I, Video 1 and 2). We conclude that KIF5B-560 can indeed acutely relocalize its own positive regulator MAP7D3, but not MAP7, when the kinesin expression is sufficiently high.

To explain why the distribution of MAP7D3 but not that of MAP7 was sensitive to the presence of kinesin-1, we hypothesized that MAP7D3 might be more mobile on MTs. To test this idea, we performed Fluorescence Recovery after Photobleaching (FRAP) experiments with GFP-tagged MAP7 and MAP7D3 and found that the latter indeed exchanged much more rapidly on MTs (Fig. 3J, K). The different turnover rates of the two MAP7 family proteins on MTs, possibly combined with the different affinities to kinesin-1, seem to contribute to their differential relocalization by overexpressed kinesin-1.

MAP7 and MAP7D3 control kinesin-1 recruitment to MTs and motor processivity

To get further insight into the similarities and differences in the regulation of kinesin-1 by MAP7 proteins, we set up in vitro reconstitution assays. In contrast to previously published experiments, which employed taxol-stabilized MTs in the absence of free tubulin, we used dynamic MTs that

were grown from GMPCPP-stabilized seeds (Bieling et al., 2007). Kinesins, MAPs and MTs were observed by Total Internal Reflection Fluorescence Microscopy (TIRFM), as described previously (van Riel et al., 2017). Using purified MAP7 and MAP7D3 labeled with Alexa 647 coupled to a SNAP-tag (Fig. S2A), we found that MAP7 showed very long static binding events, many of which exceeded our observation time (5 min) (Fig. 4A), in agreement with recently published data (Monroy et al., 2018). In contrast, MAP7D3 displayed a diffusive behavior, with many short binding events (Fig. 4A). These data are in agreement with the FRAP data, showing that in cells, MAP7D3 is more mobile than MAP7 (Fig. 3J, K). The density of MT labeling was higher with MAP7 than with MAP7D3 at the same protein concentration, indicating that the latter has a lower affinity for MTs (Fig. 4A, B and S3A).

To study kinesin-1 motility, we purified KIF5B-560-GFP from HEK293T cells (Fig. S2A). Analyses by mass spectrometry and Western blotting showed that although some co-purification of MAP7, MAP7D1 and MAP7D3 with this kinesin was observed when the protein was washed with a low ionic strength buffer, this contamination was removed when the ionic strength of the washing buffer was increased (Fig. S2B, C). We used such a “high-salt washed” KIF5B-560 preparation for all our experiments. When KIF5B-560 was added to MAP7 or MAP7D3-decorated MTs, we observed a strong (up to 23.6 fold) increase in the motor landing frequency compared to the situation with KIF5B-560 alone (Fig. 4C and D), in agreement with published data on MAP7 (Monroy et al., 2018). The landing frequency of KIF5B-560 increased with higher MAP concentrations and correlated with increasing MT labeling intensity by the particular MAP (Fig. 4B, C and S3A). Furthermore, we found that MAP7D3 but not MAP7 caused a very significant decrease in kinesin velocity (Fig. 4H and S3B). Finally, we found that both MAP7 and MAP7D3 could induce a 2 fold increase in kinesin processivity (Fig. 4D-G), with some kinesin runs exceeding 10 µm in length. We note that for this quantification, we only took into account the runs, in which we observed both kinesin association and dissociation from the MT. Inclusion of all detected runs suggested that in the presence of MAP7 or MAP7D3, even longer runs could occur (not shown).

The increase of run lengths in the presence of MAP7 and MAP7D3 could be explained by kinesin multimerization or by a model where MAP7 acts as an additional MT attachment point. In these cases the distribution of run lengths is expected to be described by the sum of two or three

exponential decays (Klumpp and Lipowsky, 2005). However, the corresponding best fit of distributions at Fig. 4F and G converged to a single exponential decay, suggesting that MAP7 directly affects kinesin's binding/unbinding rate constants, rather than introducing an additional intermediate binding state. Moreover, single molecule analysis of KIF5B-560 moving on MTs showed that the kinesin intensity profiles matched that of a single dimer in assays both with and without MAP7D3 (Fig. S3C). In addition, we performed mixed kinesin assays where GFP- and SNAP(Alexa647)-tagged kinesins were used in a 1:1 ratio. If KIF5B-560 would multimerize in the presence of MAP7 proteins, then one would expect to see a significant fraction of two-colored kinesin tracks per kymograph; however, such events were not observed (Fig. S3D), confirming our observation of KIF5B-560 behaving as a single dimer on MAP7-decorated MTs. Taken together, these data suggest that the presence of MAP7 alters the state of single kinesin dimers.

Interestingly, MAP7 could only promote kinesin processivity at high concentrations, when MTs were fully decorated, whereas MAP7D3 reduced kinesin detachment from MTs even at low concentrations (Fig. 4E-G). These data correlated with the observation that MAP7D3, but not MAP7, could move together with KIF5B-560 in vitro (Fig. 4I, J). We conclude that MAP7 proteins can affect not only kinesin landing on MTs, as suggested previously (Monroy et al., 2018; Sung et al., 2008), but also processive kinesin movement along a MT. Co-transport of the MAP with the kinesin can facilitate processive motion, but is not essential, as also a statically bound MAP can exert this effect if its density on MTs is high enough.

MAP7D3 C-terminus promotes MT recruitment and processivity of kinesin-1 in spite of having only a low MT affinity

Since our results in cells indicated that the C-terminal parts of MAP7 proteins could rescue mitochondria distribution and KIF5B-560 binding to MTs in cells lacking full length MAP7 proteins, we set out to compare the effect of MAP7D3 and its C-terminus (Ct, see Fig. 1A) on kinesin-1 motility in vitro (Fig. 5A). In agreement with a previous publication (Yadav et al., 2014), MAP7D3-Ct displayed a weak MT binding (Fig. 5B and S4A): MT labeling intensity with 20 nM MAP7D3-Ct was 19.2 fold lower than with 20 nM full length MAP7D3 (Fig. 5B and

S4A). In spite of this lower MT affinity, MAP7D3-Ct could efficiently increase KIF5B-560 landing rate, decrease its velocity and promote motor processivity (Fig. 5A-E and S4A-B). The effect of MAP7D3-Ct on the landing rate was particularly obvious at 75 nM concentration, as MT labeling at this concentration was still 8.3 fold lower than with 20 nM full length MAP7D3, whereas the KIF5B-560 landing frequency was 8.1 fold higher compared to control (kinesin only) (Fig. 5B and C). These data argue against the simple model that MAP7D3 acts as MT-recruiting factor for kinesin-1, but cannot exclude that the weak binding of MAP7D3 C-terminus to MTs augments KIF5B-560-MT interaction. These data also show that the addition of a weak MAP module to the kinesin coil is sufficient to make kinesin-1 processive.

Simultaneous imaging of KIF5B-560-GFP and mCherry-MAP7D3-Ct showed that this truncated MAP colocalized with moving kinesin (Fig. 5F). Importantly, FRAP analysis in the mCherry channel, leaving the GFP fluorescence unaffected, showed that MAP7D3-Ct exchanged rapidly on moving KIF5B-560 motors (Fig. 5F, G). This fast binding-unbinding kinetics helps to explain how static MAP7 proteins can promote processivity of KIF5B-560 (Fig. 4D-G).

MAP7 C-terminus promotes MT recruitment independently of MT binding

To investigate whether MAP7 family proteins can exert an effect on kinesin-1 that is independent of MT tethering, we sought to find a C-terminal fragment of the MAP7 protein that still interacts with kinesin-1 but does not bind to MTs. In a previous publication (Yadav et al., 2014), it has already been argued that the high number of positively charged amino acids in the MAP7D3 C-terminus contributes to MT binding, while MAP7 mostly lacks these residues. Using a MT pelleting assay, we indeed found that the MAP7 C-terminus, used before in cellular experiments (Fig. 1J, 2E and S1B) does not co-sediment with MTs (Fig. 6A and S4C). We were also unable to detect the binding of this C-terminal fragment of MAP7 tagged with mCherry to MTs in vitro by fluorescence (Fig. S4D).

Nanomolar concentrations of MAP7-Ct had no effect on KIF5B-560 behavior, as described (Metivier et al., 2018). To increase the concentration of the kinesin-binding region of MAP7 in the assay, we generated its shorter version (MAP7-Ct(mini), Fig. 1A), which could be prepared from *E.coli* at high concentration in an untagged form (Fig. S2A). When added at micromolar

concentrations to the assay with KIF5B-560, this protein fragment caused a significant (3.4 fold) increase in the motor landing frequency (Fig. 6B, C), whereas the velocity of the kinesin was only mildly affected (Fig. 6D, E). Strikingly, the increase in motor processivity observed with the MAP7D3 C-terminus was not detected with MAP7 C-terminus (Fig. 6F). It is possible that MAP7 C-terminus dissociates from the kinesin very soon after the motor lands on the MT, and since MAP7-Ct does not concentrate on MTs, the chance of its re-association with the kinesin during a run is low. Altogether, MT landing of kinesin-1 can be increased by MAP7 family proteins independent of their MT interaction, whereas the regulation of kinesin processivity by these MAPs depends on their association with MTs.

The stalk of KIF5B-560 inhibits MT interaction

Our finding that MAP7 C-terminus improves the MT landing frequency of KIF5B-560 could potentially be explained if the MAP7-interacting stalk of kinesin-1 partly interferes with MT binding. If this were true, a kinesin-1 truncation lacking this stalk should bind to MTs more efficiently. To test this idea, we generated a shorter KIF5B truncation mutant, KIF5B-370, which lacks the MAP7-binding coil region but still dimerizes via its neck linker (Fig. 1A and 7A). The concentrations of KIF5B-370 and KIF5B-560 were carefully controlled on a Coomassie blue stained gel (Fig. 7B). In in vitro assays, KIF5B-370 appeared to be a faster kinesin with slightly shorter runs compared to KIF5B-560 (Fig. S4E, F). Importantly, we observed a 7.8 fold difference in motor landing frequency (Fig. 7C, D), indicating that the presence of the stalk region in KIF5B-560 has a negative effect on its interaction with MTs.

Discussion

In this study, we have systematically analyzed the impact of mammalian MAP7 family proteins on kinesin-1 transport. We found that having at least one MAP7 homolog was necessary and sufficient to enable kinesin-1-driven distribution of mitochondria in the cytoplasm. These results are fully in agreement with the data showing that MAP7/ensconsin is an essential kinesin-1 co-factor in flies and in mammalian muscle cells (Barlan et al., 2013; Metivier et al., 2018; Metzger et al., 2012; Monroy et al., 2018; Sung et al., 2008). Dependence on MAP7 family members likely applies to many other kinesin-1-dependent processes in mammals, because the core part of kinesin-1, the KIF5B-560 fragment, was not able to bind to MTs efficiently in cells when all MAP7 homologues were absent.

Kinesin-1 function could be rescued to a significant extent by a MAP7 fragment that binds to kinesin, but not to MTs, again in agreement with the data obtained in *Drosophila* (Barlan et al., 2013; Metivier et al., 2018). KIF5B-560 recruitment to MTs could also be restored by this MAP7 fragment, and this effect could be recapitulated in vitro with purified components. Interestingly, in vitro, a short kinesin-1 version (KIF5B-370), which lacked the MAP7-binding stalk region altogether, interacted with MTs more efficiently than KIF5B-560. These data suggest that the stalk might partially inhibit MT binding, and that this effect could be relieved by the interaction with MAP7. It is possible that the stalk-containing kinesin can adopt conformations that are unfavorable for MT binding, whereas the interaction with MAP7 allosterically stabilizes a conformation that promotes MT engagement (Fig. 7E,F). Diverse regulatory steps have been described for kinesin-1, mostly involving the autoinhibitory C-terminal tail region (reviewed in (Verhey and Hammond, 2009) and also the motor domain (Xu et al., 2012)). Our data add to this complexity by showing that the state or the position of the stalk and its binding partners might directly affect the interactions between the motor domains of kinesin-1 and MTs.

Although a MAP7 fragment lacking MT affinity can make kinesin-1 more active, the presence of the MT binding domain makes this regulation much more efficient and robust, as without it, a very high concentration of MAP7 kinesin-binding domain is required to activate the motor. The presence of a MT-binding site, even a weak one (such as the one in the MAP7D3-Ct), concentrates the kinesin-binding domain of the MAP on MTs and can thus facilitate its interaction with the kinesin (Fig. 7F). Furthermore, MT-bound MAP7 proteins have a significant

effect on kinesin processivity, and we excluded the possibility that this was due to kinesin multimerization. We note that in our in vitro assays, kinesin run length is relatively high (close to 2 µm on average) even in the absence of cofactors. One possible reason for this is the fact that we work with dynamic MTs in the presence of soluble tubulin, as opposed to standard assays with taxol-stabilized MTs in the absence of tubulin. We thus observe kinesin behavior on freshly formed MT lattices, which might have fewer defects, and even if damaged, can possibly be repaired by tubulin incorporation (Schaedel et al., 2015).

We found that both a very immobile MAP (MAP7) and a more dynamic and diffusively behaving MAP (MAP7D3) could enhance kinesin-1 processivity, but the latter was able to exert this effect when present on a MT at a lower density. Some affinity of the kinesin-bound MAP fragment to MTs was required to increase motor processivity, and this could suggest that, unlike the landing rate, kinesin processivity is governed not just by the motor conformation but by the presence of additional links to MTs. However, the analysis of the run lengths of KIF5B-560 in the presence of MAP7 proteins showed that their distribution was monoexponential, whereas a significant contribution of an additional MAP-dependent MT bound state would be expected to lead to a distribution corresponding to the sum of two or three exponential decays (Klumpp and Lipowsky, 2005). We thus favor the idea that the interaction with MAP7 alters the kinesin conformation, making it more favorable for MT binding, and this is reflected in both higher landing rates and longer run lengths (Fig. 7E). Since the interaction of MAP7 with the kinesin is transient, its MT-unattached version (MAP7-Ct) would dissociate very rapidly after landing, and this fragment thus cannot enhance kinesin processivity. In contrast, MT-tethered full length MAP7 proteins or the MAP7D3 C-terminus have a much higher local concentration, which promotes repeated interactions with the kinesin and its maintenance in a state favorable for MT binding. In this way, the rapid binding-unbinding kinetics, which could be described as kinesin “hopping” from one stationary MAP molecule to another, can allow an immobile MAP7 to counteract kinesin dissociation without strongly affecting motor velocity.

MAP7D3 is different from MAP7 because it binds to MTs less tightly and can be “dragged” with the motor to some extent, which possibly explains why it slows down kinesin movement and why its low concentration, which had only a mild effect on the kinesin landing frequency, was sufficient to increase motor processivity (Fig. 4 and 7E). However, because of the fast turnover

within the MAP-motor complex, MAP7D3 is unlikely to be undergoing large-distance transport by the kinesin. MAP7D3 can be relocalized to MT plus ends by KIF5B-560 quite rapidly, but only when the motor is overexpressed. At the endogenous kinesin-1 expression levels, MAP7D3 is not enriched at MT plus ends, suggesting that the levels of endogenous motor are insufficient to drive MAP7D3 to the cell periphery. Still, it is possible that also the endogenous kinesin-1 causes some redistribution of MAP7D3, thus contributing to the localization of its own positive regulator. It has been suggested that MAP7 and MAP7D1 can undergo MT plus end-directed displacement in migrating cells (Kikuchi et al., 2018), and therefore, the dependence of the localization of these MAPs on the presence of the kinesin deserves further investigation.

An important question is whether the distribution of MAP7 proteins contributes to the well-documented selectivity of kinesin-1 for specific MT tracks, which appear to correspond to the stable, long-lived MT population (Cai et al., 2009; Farias et al., 2015; Guardia et al., 2016; Hammond et al., 2008; Jacobson et al., 2006; Nakata and Hirokawa, 2003; Tas et al., 2017). The idea that MAP7 proteins can spatially control kinesin-1 activity is supported by our observation that overexpressed KIF5B-560 accumulates in cell corners only in the presence of MAP7D3, which can be shifted by the kinesin towards MT plus ends. In contrast, MAP7, which is stably associated with MTs, does not support this peripheral localization of KIF5B-560. A MAP with a slow turnover, such as MAP7, could in principle predispose kinesin-1 for interacting with more long-lived MTs, on which this MAP would gradually accumulate, a possibility that would be interesting to test.

Finally, it would be interesting to know whether MAP7 proteins exert similar regulatory effects on any other kinesins, and thus whether the mechanism described here is shared by other motors. Taken together, our data illustrate the complexity of the interplay between the motors and the tracks they use during intracellular transport processes.

Materials and Methods

Cell Culture, knockdowns and CRISPR/Cas9 knockouts

HeLa (Kyoto), Cos7 and human embryonic kidney 239T (HEK293T) cell lines were cultured in medium that consisted of 45% DMEM, 45% Ham's F10, and 10% fetal calf serum supplemented with penicillin and streptomycin. The cell lines were routinely checked for mycoplasma contamination using LT07-518 Mycoalert assay (Lonza). HeLa and COS7 cells were transfected with plasmids using FuGENE 6 (Promega) for generating knockout lines, live cell imaging and immunofluorescence experiments. For streptavidin pull down assays and protein purification from HEK293T cells, plasmids were transfected with polyethylenimine (PEI; Polysciences). For generating knockdowns, HeLa cells were transfected with 100 nM siRNA for each target using HiPerfect (Qiagen). The following siRNAs were used in this study: MAP7D1 (target sequence 5'-TCATGAAGAGGACTCGGAA-3'), MAP7D3 (target sequence 5'-AACCTACATTCGTCTACTGAT-3') and luciferase (target sequence 5'-TCGAAGTATTCCGCGTACG -3'). For rescue experiments, HeLa cells were transfected 2 days after siRNA transfection.

HeLa CRISPR/Cas9 knockout lines were generated using the pSpCas9-2A-Puro (PX459) vector, purchased from Addgene (Ran et al., 2013). Guide RNAs for human KIF5B, MAP7, and MAP7D3 were designed using the CRISPR design webpage tool (http://crispr.mit.edu). The targeting sequences for gRNAs were as follows (coding strand sequence indicated): KIF5B, 5′-CCGATCAAATGCATAAGGCT-3′; MAP7, 5′-CGCCCTGCCTCTGCAATTTC-3′; MAP7D3, 5′-CCGTGCCCGCAGCTCTCTCA-3′. The CRISPR/Cas9-mediated KIF5B, MAP7, and MAP7D3 knockout was performed according to the protocol described in (Ran et al., 2013). In brief, HeLa cells were transfected using Fugene6 (Promega) with the vectors bearing the appropriate targeting sequences. Cells were subjected to selection with 2 µg/ml puromycin 24-48 hours post transfection for 48-72 hours. After selection, cells were allowed to recover in complete medium for approximately 7 days; meanwhile, cells were diluted in 96 wells plates for growing single cell colonies, and knockout efficiency was checked using the mixed cell population by immunofluorescence staining. Depending on knockout efficiency, 5-30 individual clones were isolated and characterized by Western blotting and immunostaining.

DNA constructs

All MAP7 family protein constructs were cloned by a PCR-based strategy into a Bio-mCherry-C1 vector, except for MAP7D1-FL which has been cloned into a Bio-mCherry-C3 vector. MAP7 constructs were generated from HeLa cell cDNA. MAP7D1 was cloned based on cDNA of IMAGE clone 6514558 (Source Bioscience), MAP7D2 was cloned based on cDNA of IMAGE clone 3063898 (Source Bioscience) and MAP7D3 was cloned based on cDNA of IMAGE clone 5284128 (Source Bioscience). Rescue constructs for MAP7D1 and MAP7D3 were obtained by PCR-based mutagenesis of the sequence TCATGAAGAGGACTCGGAA to TCATGAAGAGAACACGCAA (MAP7D1) and AACCTACATTCGTCTACTGAT to AATCTACACTCGTCTACAGAT (MAP7D3). For protein purification from HEK293T cells, MAP7-Ct was cloned into a pmCherry-C1 vector with an N-terminal Strep-tag, and full-length MAP7 and MAP7D3 were cloned into a pTT5 vector with N-terminal SNAP- and Strep-tag. For bacterial purifications, MAP7D3 constructs were cloned into a pET28a vector containing N-terminal Strep-tag. MAP7-Ct (mini) construct was cloned by a PCR-based strategy into a pET24a vector containing an N-terminal SUMO-tag. All KIF5B constructs were cloned by a PCR-based strategy into pEGFP-N1 vectors. K560-GFP used for protein purification was cloned into a pTT5 vector with a C-terminal Strep-tag. K370-GFP used for protein purification was cloned into a pEGFP-N1 vector with a C-terminal Strep-tag. All kinesin constructs were based on full length human KIF5B as template IMAGE clone 8991997 (van Spronsen et al., 2013). KIF5B-mCherry-LexyC was cloned by PCR-based strategy. A c-myc NLS sequence was introduced between K560 and mCherry (amino acid sequence: PAAKRVKLD) and a second SV40 Large T-antigen nuclear localization signal (NLS) was introduced between mCherry and the LEXY domain (amino acid sequence: PKKKRKV). The engineered LOV2-domain (LEXY) for blue light-inducible nuclear export was obtained from Addgene (catalog #72655) (Niopek et al., 2016). Biotin ligase BirA expression construct (Driegen et al., 2005) was a kind gift from D. Meijer (University of Edinburgh, UK).

Immunostainings, Western blotting and antibodies

For immunofluorescence cell staining, HeLa cells were fixed in –20°C methanol for 10 min and stained for MAP7, MAP7D1, MAP7D2, MAP7D3 and α-tubulin. In the case of cytochrome c, cells were fixed with 4% PFA in phosphate-buffered saline (PBS) for 10 min. Cells were then permeabilized with 0.15% Triton X-100 in PBS for 2 min; subsequent wash steps were performed in PBS supplemented with 0.05% Tween-20. Epitope blocking and antibody labeling steps were performed in PBS supplemented with 0.05% Tween-20 and 1% BSA. Before mounting in Vectashield mounting medium (Vector Laboratories) slides were washed with 70% and 100% ethanol and air-dried.

For immunofluorescence cell staining and Western blotting, we used rabbit polyclonal antibodies against MAP7D1 (HPA028075, Sigma/Atlas), MAP7D2 (HPA051508, Sigma/Atlas), MAP7D3 (HPA035598, Sigma/Atlas), Kinesin heavy chain (UKHC H-50, SC28538, Santa Cruz) and GFP (ab290; Abcam). We used a mouse polyclonal antibody against MAP7 (H00009053-B01P, Abnova) and mouse monoclonal antibodies against Ku80 (611360, BD Bioscience), mCherry (632543, Clontech), Cytochrome c (556432, BD Bioscience) and α-tubulin (T6199, Sigma), and a rat monoclonal antibody against α-tubulin (γL1/2, ab6160, Abcam). The following secondary antibodies were used: IRDye 800CW/680LT goat anti–rabbit, and anti–mouse for Western blotting and Alexa Fluor 488–, 594–, and 647–conjugated goat antibodies against rabbit, rat, and mouse IgG (Molecular Probes) for immunofluorescence. Mitotracker Red CMXRos (Molecular Probes) was alternatively used for mitochondria staining.

Total HeLa cell extracts were prepared in RIPA buffer containing 50 mM Tris-HCl pH 7.5, 150 mM NaCl, 1% Triton X-100, 0,5% SDS and cOmplete protease inhibitor cocktail (Roche).

Pull down assays

Streptavidin pull down assays were performed from HEK293T cell lysates by coexpressing biotin ligase BirA with mCherry-tagged constructs containing a biotinylation site (BirA substrate sequence: MASGLNDIFEAQKIEWHEGGG) (bait), and a GFP-tagged KIF5B construct (prey). Constructs were transfected altogether into HEK293 cells using PEI with 24 hrs incubation time for proper protein expression. M-280 Streptavidin Dynabeads (Invitrogen) were blocked in a buffer containing 20 mM Tris pH 7.5, 20% glycerol, 150 mM NaCl, and 10 µg Chicken Egg

Albumin followed by three washes with wash buffer containing 20 mM Tris pH 7.5, 150 mM NaCl and 0.1% Triton-X. HEK293T cells were scraped and collected in ice-cold PBS followed by lysis on ice in a buffer containing 20 mM Tris pH 7.5, 150 mM NaCl, 1mM $MgCl_2$, 1% Triton X-100, and cOmplete protease inhibitor cocktail (Roche). To separate cell debris, the lysates were pelleted 4 ^{o}C for 15 min at 16000 g and 10 % of each lysate was saved as input control. Cell lysates were incubated with pre-blocked streptavidin beads for 60 min at 4 ^{o}C followed by five washes with wash buffer containing 20 mM Tris pH 7.5, 150 mM NaCl and 0.1% Triton-X. Streptavidin beads were pelleted and boiled in 2x Laemmli sample buffer. Protein lysates and pull down of both bait and prey proteins were analyzed by Western blot.

Protein Purification

All KIF5B, SNAP(Alexa647)-labeled proteins and mCherry-MAP7-Ct used for in vitro reconstitution assays were purified from HEK293T cells using Strep(II)-streptactin affinity purification. Cells were harvested 24-40 hrs post transfection. Cells from a 15 cm cell culture dish were lysed in 800 µl of lysis buffer containing 50 mM HEPES pH 7.4, 300 mM NaCl, 1mM $MgCl_2$, 1mM DTT and 0.5% Triton X-100, supplemented with cOmplete protease inhibitor cocktail (Roche) on ice for 15 min. The supernatant obtained from the cell lysate after centrifugation at 16000 x g for 20 min was incubated with 50 µl of StrepTactin Sepharose beads (GE Healthcare) for 1 hr. The beads were washed 5 times in a high-salt wash buffer containing 50 mM HEPES pH 7.4, 1.5 M NaCl, 1 mM $MgCl_2$, 1 mM EGTA, 1 mM DTT, and 0.05% Triton X-100 and three times with an elution wash buffer containing containing 50 mM HEPES pH 7.4, 150 mM NaCl, 1 mM $MgCl_2$, 1 mM EGTA, 1 mM DTT and 0.05% Triton X-100. The proteins were eluted with 40-150 µl of elution buffer containing 50 mM HEPES pH 7.4, 150 mM NaCl, 1 mM $MgCl_2$, 1 mM EGTA, 1 mM DTT, 2.5 mM d-Desthiobiotin and 0.05% Triton X-100. To label SNAP-tagged proteins with SNAP-Surface Alexa Fluor 647 (NEB), 20–40 µM dye was incubated with proteins on beads for 1 hr between wash and elution steps. After extensive washing, proteins were eluted in the elution buffer with 300 mM instead of 150 mM NaCl. Concentration of purified proteins were measured by BSA standard on SDS gel. All purified proteins were snap frozen in liquid nitrogen and stored in −80 °C.

For protein purification of MAP7D3 constructs from bacteria, BL21 *E.coli* were transformed with the respective MAP7D3 construct. Bacteria were grown till OD600 of 0.6 at 37°C after which protein expression was induced with 1 mM IPTG for 1 hr at 37 ^{o}C and 2.5 hrs at 20 ^{o}C. Bacteria were spun down and subjected to one freeze-thaw cycle at -80 ^{o}C to stimulate proper lysis. Bacteria were resuspended and sonicated at 4 ^{o}C in cold lysis buffer containing 50 mM sodium phosphate pH 8, 250 mM NaCl, 1 mM $MgCl_2$, 1 mM DTT, 0.5% Triton X-100, 1mM PMSF and cOmplete protease inhibitor cocktail (Roche). Lysates were centrifugated at 25000 x g for 45-60 min and the supernatants were incubated with Strep-Tactin Superflow high-capacity beads (IBA Lifesciences) for 60 min at 4 ^{o}C, followed by 5 washes with a buffer containing 50 mM sodium phosphate pH 6.0, 250 mM NaCl, 1 mM $MgCl_2$ and 1 mM DTT. The proteins of interest were eluted with a buffer containing 50 mM sodium phosphate pH 7.0, 250 mM NaCl, 1 mM $MgCl_2$ 1 mM DTT and 5 µm d-Desthiotiotin. The eluted fractions were pooled and supplemented with 10% sucrose for preservation. Proteins were snap frozen and stored at -80 ^{o}C. Concentration of purified proteins were measured by BSA standard on SDS gel.

For bacterial protein purification of MAP7-Ct(mini), B21 Rosetta2 cells (Novagen) containing pET24a vector (Novagen) encoding the SUMO-MAP7-Ct(mini) truncation were cultured. 2L culture, in LB medium supplemented with antibiotic 10 mg/ml kanamycin (Sigma-Aldrich) and 33 mg/ml chloramphenicol (Sigma-Aldrich), was grown until OD600 of ~0.8-1, after which protein production was induced with 0.1 mM IPTG (Thermo Scientific). Protein production was performed overnight at 18°C. Cells were harvested by centrifugation and subjected to one freeze-thaw cycle at -80 oC to stimulate proper lysis. The pellet was thawed and resuspended in 50 mM sodium phosphate buffer pH 8.0, 150 mM NaCl, cOmplete protease inhibitor cocktail (Roche) and 5 mM β-mercaptoethanol. Cells were then disrupted by an EmulsiFlex-C5 (Avestin) cell disruptor. Lysate was cleared by centrifugation (55000 g, 45 min), filtered with a 0.22 □m polypropylene filter (VWR) and mixed for 15 min with Protino® Ni-IDA resin (Macherey-Nagel) at 4 oC. Protein was eluted with 50 mM sodium phospha¬¬te pH 8.0, 250 mM imidazole, 150 mM NaCl, cOmplete protease inhibitor cocktail (Roche) and 5 mM β-mercaptoethanol. Eluate was then digested by Ulp1 overnight at 4°C while dialyzed against 50mM phosphate buffer pH 8.0 with a 6 kDa cut-off membrane (Spectrum Laboratories). Protein was loaded on a POROS® 20HS (Thermo Fischer Scientific) column in the same dialysis buffer, using ÄKTA® purifier (GE Healthcare) for cation exchange chromatography. Protein was eluted by a 0-100%

15 CV gradient of 2M KCl (Carl Roth); fractions of 0.5 ml were collected. Fractions of interest were then concentrated and exchanged against 25 mM HEPES buffer pH 7.5 with 75 mM KCl, 75 mM NaCl and 10 mM DTT using a Vivaspin column (cut-off: 6 kDa). Concentration was confirmed with an ND-100 spectrophotometer (Nanodrop Technologies). Purity was confirmed by SDS-PAGE and protein was aliquoted and stored at -80°C.

Mass spectrometry

After streptavidin purification, beads were resuspended in 20 µl of Laemmli sample buffer (Biorad) and supernatants were loaded on a 4-12% gradient Criterion XT Bis-Tris precast gel (Biorad). The gel was fixed with 40% methanol/10% acetic acid and then stained for 1 hr using colloidal Coomassie dye G-250 (Gel Code Blue Stain Reagent, Thermo Scientific). After in-gel digestion, samples were resuspended in 10% formic acid (FA)/5% DMSO and analyzed with an Agilent 1290 Infinity (Agilent Technologies, CA) LC, operating in reverse-phase (C18) mode, coupled to an Orbitrap Q-Exactive mass spectrometer (Thermo Fisher Scientific, Bremen, Germany). Peptides were loaded onto a trap column (Reprosil C18, 3 µm, 2 cm × 100 µm; Dr. Maisch) with solvent A (0.1% formic acid in water) at a maximum pressure of 800 bar and chromatographically separated over the analytical column (Zorbax SB-C18, 1.8 µm, 40 cm × 50 µm; Agilent) using 90 min linear gradient from 7-30% solvent B (0.1% formic acid in acetonitrile) at a flow rate of 150 nl/min. The mass spectrometer was used in a data-dependent mode, which automatically switched between MS and MS/MS. After a survey scan from 350-1500 m/z the 10 most abundant peptides were subjected to HCD fragmentation. MS spectra were acquired in high-resolution mode (R > 30,000), whereas MS2 was in high-sensitivity mode (R > 15,000). Raw files were processed using Proteome Discoverer 1.4 (version 1.4.0.288, Thermo Scientific, Bremen, Germany). The database search was performed using Mascot (version 2.4.1, Matrix Science, UK) against a Swiss-Prot database (taxonomy human). Carbamidomethylation of cysteines was set as a fixed modification and oxidation of methionine was set as a variable modification. Trypsin was specified as enzyme and up to two miss cleavages were allowed. Data filtering was performed using percolator, resulting in 1% false discovery rate (FDR). Additional filters were; search engine rank 1 peptides and ion score >20.

In vitro Reconstitution Assays

MT seeds were prepared by incubating 20 μM porcine tubulin mix containing 70% unlabeled, 18% biotin-tubulin and 12% rhodamine-tubulin with 1 mM guanylyl-(α,β)-methylenediphosphonate (GMPCPP) at 37 ^{o}C for 30 min. Polymerized MTs were separated from the mix by centrifugation in an Airfuge at 119,000 g for 5 min. MTs were subjected to one round of depolymerization and polymerization in 1 mM GMPCPP, and the final MT seeds were stored in MRB80 buffer (80 mM K-PIPES pH 6.8, 1 mM EGTA, 4 mM $MgCl_2$) containing 10% glycerol. In vitro reconstitution assays were performed in flow chambers assembled from microscopy slides and plasma cleaned coverslips. The chambers were treated with 0.2 mg/ml PLL-PEG-biotin (Surface Solutions, Switzerland) in MRB80 buffer for 5 min. After washing with the assay buffer, they were incubated with 1 mg/ml NeutrAvidin for 5 min. MT seeds were attached to the biotin-NeutrAvidin links and incubated with 1 mg/ml κ-casein. The in vitro reaction mixture consisted of 20 μM tubulin, 50 mM KCl, 0.1% Methylcellulose, 0.5 mg/ml κ-casein, 1 mM GTP, oxygen scavenging system (20 mM glucose, 200 μg/ml catalase, 400 μg/ml glucose-oxidase, 4 mM DTT), 2 mM ATP, 0.2 - 10 nM of respective kinesin (concentrations were calculated for monomeric proteins) and MAP7 or MAP7D3 at indicated concentrations. After centrifugation in an Airfuge for 5 min at 119,000 g, the reaction mixture was added to the flow chamber containing the MT seeds and sealed with vacuum grease. The experiments were conducted at 30 ^{o}C and data were collected using TIRF microscopy. For some experiments without mCherry-labeled MAP7/MAP7D3, the reaction mixture was composed of 19.5 μM tubulin supplemented with 0.5 μM rhodamine-labeleld tubulin. All tubulin products were purchased from Cytoskeleton Inc.

For MT pelleting assays a reaction containing 37.5 μM porcine brain tubulin supplemented with 1mM GTP, 1mM DTT and 20 μM Taxol in MRB80 was prepared at 30 ^{o}C for 30 min. The reaction was divided and supplemented with MRB80 buffer with or without mCherry-MAP7-Ct at a final tubulin concentration of 30 μM. Also a control without tubulin was included. Subsequently, all reactions were incubated for another 15 min at 30 ^{o} C. Pelleting was performed in an Airfuge at 119,000 g with a pre-warmed rotor for 10 min. Supernatants were removed and pellets were resuspended in MRB80 buffer on ice by regular pipetting for 40 min. All samples were supplemented with 4x Laemmli sample buffer, boiled and analyzed by SDS-PAGE.

Single molecule intensity analysis

Single molecule fluorescence histograms of monomeric GFP (control) or kinesins moving on MT lattices were built from acquisitions made on a TIRF microscope. To ensure identical imaging conditions, a single imaging slide (with a plasma cleaned coverslip) was used containing three flow chambers to image GFP (control) and K560-GFP (with or without MAP7 proteins). For purified GFP, proteins were diluted in MRB80 and added to an imaging flow chambers; chambers were subsequently washed with MRB80, leaving a fraction of the GFP proteins immobilized on the coverslip. Protein dilution was optimized to provide images of approximately 0.01 fluorophores per µm2 for GFP control conditions. To estimate the number of GFP molecules per kinesin, an in vitro reconstitution assay with KIF5B-560-GFP moving on MTs in the presence or absence of MAP7 proteins was setup in the remaining two flow chambers as described before. After sealing with vacuum grease to prevent evaporation, samples were imaged at 30 ^{o} C. For monomeric GFP, approximately 100 images were acquired at different positions on the coverslip to avoid pre-bleaching. For moving kinesins, approximately 5-10 movies were obtained where only the first 10 frames were analyzed to prevent analyzing extensive photobleaching. All acquisitions were obtained under identical laser power, exposure time and TIRF angle. ImageJ plugin Comdet v.0.3.6.1 and DoM_Utrecht v.1.1.5 https://github.com/ekatrukha/DoM_Utrecht) were used for detection and fitting of single molecule fluorescent spots as described previously (Yau et al., 2014). In short, individual spots were fitted with 2D Gaussian and the amplitude of the fitted Gaussian function was used as a measure of the fluorescence intensity value of an individual spot. The histograms were fitted to lognormal distributions using GraphPad Prism 7.

Image acquisition and processing

Fixed cells were imaged with a Nikon Eclipse 80i upright fluorescence microscope equipped with Plan Apo VC N.A. 1.40 oil 100x and 60x objectives, or Nikon Eclipse Ni-E upright fluorescence microscope equipped with Plan Apo Lambda 100x N.A. 1.45 oil and 60x N.A. 1.40 oil objectives microscopes, Chroma ET-BFP2, - GFP, -mCherry, or -Cy5 filters and Photometrics CoolSNAP

HQ2 CCD (Roper Scientific, Trenton, NJ) camera. The microscopes were controlled by Nikon NIS Br software.

FRAP and LEXY optogenetic experiments were done using spinning disk microscopy, which was performed on an inverted research microscope Eclipse Ti-E with the Perfect Focus System (Nikon), equipped with Plan Apo VC 100x N.A. 1.40 and Plan Apo 60x N.A. 1.40 oil objectives, a Yokogawa CSU-X1-A1 confocal head with 405-491-561 triple-band mirror and GFP, mCherry, and GFP/mCherry emission filters (Chroma), ASI motorized stage MS-2000-XYZ with Piezo Top Plate (ASI), a Photometrics Evolve 512 electron-multiplying charge-coupled device (CCD) camera (Photometrics), and controlled by MetaMorph 7.7 software (Molecular Devices). The microscope was equipped with a custom-ordered illuminator (MEY10021; Nikon) modified by Roper Scientific France/PICT-IBiSA, Institut Curie. Cobolt Calypso 491 nm (100 mW) and Cobolt Jive 561 nm (100 mW) lasers (Cobolt) were used as light sources. To keep cells at 37°C, we used a stage top incubator (model INUBG2E-ZILCS; Tokai Hit).

All in vitro reconstitution assays were performed on an inverted research microscope Nikon Eclipse Ti-E (Nikon) with the perfect focus system (PFS) (Nikon), equipped with Nikon CFI Apo TIRF 100 × 1.49 N.A. oil objective (Nikon, Tokyo, Japan), Photometrics Evolve 512 EMCCD (Roper Scientific) and Photometrics CoolSNAP HQ2 CCD (Roper Scientific) and controlled with MetaMorph 7.7 software (Molecular Devices, CA). The microscope was equipped with TIRF-E motorized TIRF illuminator modified by Roper Scientific France/PICT-IBiSA, Institut Curie. For excitation lasers we used 491 nm 100 mW Stradus (Vortran), 561 nm 100 mW Jive (Cobolt) and 642 nm 110 mW Stradus (Vortran). We used an ET-GFP 49002 filter set (Chroma) for imaging of proteins tagged with GFP, an ET-mCherry 49008 filter set (Chroma) for imaging X-Rhodamine labelled tubulin or mCherry-tagged proteins and an ET-405/488/561/647 for imaging SNAP-Alexa647. For simultaneous imaging of green and red fluorescence we used an Evolve512 EMCCD camera (Photometrics), ET-GFP/mCherry filter cube (59022, Chroma) together with an Optosplit III beamsplitter (Cairn Research Ltd) equipped with double emission filter cube configured with ET525/50m, ET630/75m and T585lprx (Chroma). For simultaneous imaging of green, red and far-red fluorescence we used an Evolve512 EMCCD camera (Photometrics), quad TIRF polychroic ZT405/488/561/640rpc (Chroma) and quad laser emission filter ZET405/488/561/635m (Chroma), mounted in the metal cube (Chroma, 91032) together with an

Optosplit III beamsplitter (Cairn Research Ltd) equipped with triple emission filter cube configured with ET525/50m, ET630/75m, ET700/75m emission filters and T585lprx and T660lprx dichroic (Chroma). To keep in vitro samples at 30°C, we used a stage top incubator (model INUBG2E-ZILCS; Tokai Hit).

Images and movies were processed using ImageJ. All images were modified by linear adjustments of brightness and contrast. Maximum intensity projections were made using z projection. Kinesin velocities, run lengths and landing frequencies were obtained from kymograph analysis, using ImageJ plugin KymoResliceWide v.0.4. https://github.com/ekatrukha/KymoResliceWide; copy archived at https://github.com/elifesciences-publications/KymoResliceWide). Kinesin runs <0.5 sec were included for landing frequency analysis but not analyzed for run length and velocity. Kinesins running on GMPCPP MT seeds were excluded from our analysis as much as possible. Kinesin runs >2.0 sec were analyzed for MAP7/MAP7D3 co-transport events.

For quantifying mitochondria in different HeLa cell knockdown/knockout conditions we classified mitochondria as “clustered” when ~80% of the cytochrome c signal was localized in a dense cluster around the nucleus, all other localization patterns with more spread mitochondria were classified as “spread”. K560-GFP was classified as localized on corner MTs when clear enhancement of fluorescent signal was seen at peripheral MTs near the cell cortex over MTs that are localized in between the cortex and the cell center.

FRAP measurements were performed by bleaching a 10 x 10 µm square region in a cytoplasmic region between the nucleus and cell cortex followed by 8.5 min imaging with a frame interval of 3 sec. Mean fluorescence intensities were measured from a 4 x 4 µm square region within the original photobleached region to avoid analyzing non-bleached MTs that could slide into the analyzed region. The mean intensity of this region was double corrected for background fluorescence and photobleaching (Phair et al., 2004).

Optogenetic experiments with blue light-inducible K560-LEXY kinesin were performed using spinning disk microscopy. Acquisitions were done with a frame interval of 5 sec after sequential exposure with green light 561 nm laser (to image kinesin) followed by blue light 491 nm laser (to image MAPs and activate K560-LEXY simultaneously). Exposure times of ~ 1 sec per interval

with the 491 nm laser were sufficient to actively export optogenetic motors from the nucleus. For measuring fluorescence intensity changes at cell corners, a maximum intensity projection over time of the K560-LEXY channel was made using ImageJ, followed by Gaussian blurring and thresholding to select cell corners to analyze. Mean fluorescence values for GFP-MAP7/MAP7D3 and K560-LEXY were obtained from the same cell corners over time, background subtracted and normalized to the mean fluorescence in that region at T = 0 min. Changes in mean fluorescence intensity were plotted per cell corner.

Statistical analysis

Statistical significance was analyzed either using the Mann-Whitney U test or Student's t test, as indicated in figure legends. For the t test, data distribution was assumed to be normal, but this was not formally tested. Statistical significance was determined using GraphPad Prism software (version 7.04). Fitting of run lengths with sum of two or three exponential decays was performed on the raw data using maximum likelihood estimation method implemented in *mle* function of MATLAB R2011b (The MathWorks, Natick, 2011).

Online supplemental material

Fig. S1 shows wide field images of overexpressed MAP7D3-Ct in cells stained with MitoTracker and overexpressed Nt and Ct constructs of MAP7, MAP7D1 and MAP7D3 together with K560-GFP, all in HeLa cells depleted from all three MAP7 proteins. Fig. S2 gives an overview of all purified proteins used in this study and the analysis of K560-GFP purification contaminants. Fig. S3 and S4 show binding of MAP7 proteins to MTs in in vitro reconstitution assays. Additional quantifications of kinesin behavior from Fig. 4 – 7 are included in Fig. S3 and S4. Uncropped images of the MT pelleting assay are shown in Figure S4C. Supplemental videos illustrate that MAP7D3 but not MAP7 can be rapidly relocalized by KIF5B-560 to the cell periphery.

Acknowledgments

We thank A. Aher for the help on protein purifications and D. Meijer for the gift of materials. This work was supported by the European Research Council Synergy grant 609822 and Netherlands Organization for Scientific Research ALW Open Program grant 824.15.017 to A.A., the Marie Curie IEF fellowships to M.M.

The authors declare no competing financial interests.

Author Contributions

Author contributions: P.J H. and M. M. designed, conducted and analyzed the experiments and wrote the paper. G-J.K., C.A.E.P., D.G.F.V. and W,E.vR. contributed to cellular experiments. E.A. K. contributed to data analysis. L. F. and S.G.D.R. contributed to protein purifications. A.F.M.A. and R.S. performed and analyzed mass spectrometry experiments. C.C.H. provided project feedback. L.C.K. contributed to data analysis and paper writing; A. A. supervised the study and wrote the paper.

References

Akhmanova, A., and J.A. Hammer, 3rd. 2010. Linking molecular motors to membrane cargo. *Curr Opin Cell Biol*. 22:479-487.

Barlan, K., W. Lu, and V.I. Gelfand. 2013. The microtubule-binding protein ensconsin is an essential cofactor of kinesin-1. *Curr Biol*. 23:317-322.

Bieling, P., L. Laan, H. Schek, E.L. Munteanu, L. Sandblad, M. Dogterom, D. Brunner, and T. Surrey. 2007. Reconstitution of a microtubule plus-end tracking system in vitro. *Nature*. 450:1100-1105.

Bieling, P., I.A. Telley, and T. Surrey. 2010. A minimal midzone protein module controls formation and length of antiparallel microtubule overlaps. *Cell*. 142:420-432.

Bulinski, J.C., and A. Bossler. 1994. Purification and characterization of ensconsin, a novel microtubule stabilizing protein. *J Cell Sci*. 107 (Pt 10):2839-2849.

Cai, D., D.P. McEwen, J.R. Martens, E. Meyhofer, and K.J. Verhey. 2009. Single molecule imaging reveals differences in microtubule track selection between Kinesin motors. *PLoS Biol*. 7:e1000216.

Case, R.B., D.W. Pierce, N. Hom-Booher, C.L. Hart, and R.D. Vale. 1997. The directional preference of kinesin motors is specified by an element outside of the motor catalytic domain. *Cell*. 90:959-966.

Dixit, R., J.L. Ross, Y.E. Goldman, and E.L. Holzbaur. 2008. Differential regulation of dynein and kinesin motor proteins by tau. *Science*. 319:1086-1089.

Driegen, S., R. Ferreira, A. van Zon, J. Strouboulis, M. Jaegle, F. Grosveld, S. Philipsen, and D. Meijer. 2005. A generic tool for biotinylation of tagged proteins in transgenic mice. *Transgenic Res*. 14:477-482.

Ebneth, A., R. Godemann, K. Stamer, S. Illenberger, B. Trinczek, and E. Mandelkow. 1998. Overexpression of tau protein inhibits kinesin-dependent trafficking of vesicles, mitochondria, and endoplasmic reticulum: implications for Alzheimer's disease. *J Cell Biol*. 143:777-794.

Farias, G.G., C.M. Guardia, D.J. Britt, X. Guo, and J.S. Bonifacino. 2015. Sorting of Dendritic and Axonal Vesicles at the Pre-axonal Exclusion Zone. *Cell Rep*. 13:1221-1232.

Fu, M.M., and E.L. Holzbaur. 2014. Integrated regulation of motor-driven organelle transport by scaffolding proteins. *Trends Cell Biol*. 24:564-574.

Gallaud, E., R. Caous, A. Pascal, F. Bazile, J.P. Gagne, S. Huet, G.G. Poirier, D. Chretien, L. Richard-Parpaillon, and R. Giet. 2014. Ensconsin/Map7 promotes microtubule growth and centrosome separation in Drosophila neural stem cells. *J Cell Biol*. 204:1111-1121.

Guardia, C.M., G.G. Farias, R. Jia, J. Pu, and J.S. Bonifacino. 2016. BORC Functions Upstream of Kinesins 1 and 3 to Coordinate Regional Movement of Lysosomes along Different Microtubule Tracks. *Cell Rep*. 17:1950-1961.

Gumy, L.F., E.A. Katrukha, I. Grigoriev, D. Jaarsma, L.C. Kapitein, A. Akhmanova, and C.C. Hoogenraad. 2017. MAP2 Defines a Pre-axonal Filtering Zone to Regulate KIF1- versus KIF5-Dependent Cargo Transport in Sensory Neurons. *Neuron*. 94:347-362.

Hammond, J.W., D. Cai, and K.J. Verhey. 2008. Tubulin modifications and their cellular functions. *Curr Opin Cell Biol*. 20:71-76.

Hirokawa, N., and Y. Tanaka. 2015. Kinesin superfamily proteins (KIFs): Various functions and their relevance for important phenomena in life and diseases. *Exp Cell Res*. 334:16-25.

Jacobson, C., B. Schnapp, and G.A. Banker. 2006. A change in the selective translocation of the Kinesin-1 motor domain marks the initial specification of the axon. *Neuron*. 49:797-804.

Kikuchi, K., A. Nakamura, M. Arata, D. Shi, M. Nakagawa, T. Tanaka, T. Uemura, T. Fujimori, A. Kikuchi, A. Uezu, Y. Sakamoto, and H. Nakanishi. 2018. Map7/7D1 and Dvl form a feedback loop that facilitates microtubule remodeling and Wnt5a signaling. *EMBO Rep*. 19.

Klumpp, S., and R. Lipowsky. 2005. Cooperative cargo transport by several molecular motors. *Proc Natl Acad Sci U S A*. 102:17284-17289.

Kwon, H.J., J.E. Park, H. Song, and C.Y. Jang. 2016. DDA3 and Mdp3 modulate Kif2a recruitment onto the mitotic spindle to control minus-end spindle dynamics. *J Cell Sci*. 129:2719-2725.

Lipka, J., L.C. Kapitein, J. Jaworski, and C.C. Hoogenraad. 2016. Microtubule-binding protein doublecortin-like kinase 1 (DCLK1) guides kinesin-3-mediated cargo transport to dendrites. *EMBO J*. 35:302-318.

Liu, J.S., C.R. Schubert, X. Fu, F.J. Fourniol, J.K. Jaiswal, A. Houdusse, C.M. Stultz, C.A. Moores, and C.A. Walsh. 2012. Molecular basis for specific regulation of neuronal kinesin-3 motors by doublecortin family proteins. *Mol Cell*. 47:707-721.

McHedlishvili, N., H.K. Matthews, A. Corrigan, and B. Baum. 2018. Two-step interphase microtubule disassembly aids spindle morphogenesis. *BMC Biol*. 16:14.

Metivier, M., B. Monroy, E. Gallaud, R. Caous, A. Pascal, L. Richard-Parpaillon, A. Guichet, K. Ori-McKenney, and R. Giet. 2018. The Kinesin-1 binding domain of Ensconsin/MAP7 promotes Kinesin-1 activation in vivo. *BioRxiv*:325035.

Metzger, T., V. Gache, M. Xu, B. Cadot, E.S. Folker, B.E. Richardson, E.R. Gomes, and M.K. Baylies. 2012. MAP and kinesin-dependent nuclear positioning is required for skeletal muscle function. *Nature*. 484:120-124.

Monroy, B.Y., D.L. Sawyer, B.E. Ackermann, M.M. Borden, T.C. Tan, and K.M. Ori-McKenney. 2018. Competition between microtubule-associated proteins directs motor transport. *Nat Commun*. 9:1487.

Nagaraj, N., J.R. Wisniewski, T. Geiger, J. Cox, M. Kircher, J. Kelso, S. Paabo, and M. Mann. 2011. Deep proteome and transcriptome mapping of a human cancer cell line. *Mol Syst Biol*. 7:548.

Nakata, T., and N. Hirokawa. 2003. Microtubules provide directional cues for polarized axonal transport through interaction with kinesin motor head. *J Cell Biol*. 162:1045-1055.

Niida, Y., and A. Yachie. 2011. MAP7D2 is a brain expressing X-linked maternal imprinted gene in humans. *Nature Precedings*:http://hdl.handle.net/10101/npre.12011.16684.10101.

Niopek, D., P. Wehler, J. Roensch, R. Eils, and B. Di Ventura. 2016. Optogenetic control of nuclear protein export. *Nat Commun*. 7:10624.

Phair, R.D., P. Scaffidi, C. Elbi, J. Vecerova, A. Dey, K. Ozato, D.T. Brown, G. Hager, M. Bustin, and T. Misteli. 2004. Global nature of dynamic protein-chromatin interactions in vivo: three-dimensional genome scanning and dynamic interaction networks of chromatin proteins. *Mol Cell Biol*. 24:6393-6402.

Ran, F.A., P.D. Hsu, J. Wright, V. Agarwala, D.A. Scott, and F. Zhang. 2013. Genome engineering using the CRISPR-Cas9 system. *Nat Protoc*. 8:2281-2308.

Schaedel, L., K. John, J. Gaillard, M.V. Nachury, L. Blanchoin, and M. Thery. 2015. Microtubules self-repair in response to mechanical stress. *Nat Mater*. 14:1156-1163.

Seitz, A., H. Kojima, K. Oiwa, E.M. Mandelkow, Y.H. Song, and E. Mandelkow. 2002. Single-molecule investigation of the interference between kinesin, tau and MAP2c. *EMBO J*. 21:4896-4905.

Semenova, I., K. Ikeda, K. Resaul, P. Kraikivski, M. Aguiar, S. Gygi, I. Zaliapin, A. Cowan, and V. Rodionov. 2014. Regulation of microtubule-based transport by MAP4. *Mol Biol Cell*. 25:3119-3132.

Subramanian, R., S.C. Ti, L. Tan, S.A. Darst, and T.M. Kapoor. 2013. Marking and measuring single microtubules by PRC1 and kinesin-4. *Cell*. 154:377-390.

Sun, X., X. Shi, M. Liu, D. Li, L. Zhang, X. Liu, and J. Zhou. 2011. Mdp3 is a novel microtubule-binding protein that regulates microtubule assembly and stability. *Cell Cycle*. 10:3929-3937.

Sung, H.H., I.A. Telley, P. Papadaki, A. Ephrussi, T. Surrey, and P. Rorth. 2008. Drosophila ensconsin promotes productive recruitment of Kinesin-1 to microtubules. *Dev Cell*. 15:866-876.

Syred, H.M., J. Welburn, J. Rappsilber, and H. Ohkura. 2013. Cell cycle regulation of microtubule interactomes: multi-layered regulation is critical for the interphase/mitosis transition. *Mol Cell Proteomics*. 12:3135-3147.

Tanaka, Y., Y. Kanai, Y. Okada, S. Nonaka, S. Takeda, A. Harada, and N. Hirokawa. 1998. Targeted disruption of mouse conventional kinesin heavy chain, kif5B, results in abnormal perinuclear clustering of mitochondria. *Cell*. 93:1147-1158.

Tas, R.P., A. Chazeau, B.M.C. Cloin, M.L.A. Lambers, C.C. Hoogenraad, and L.C. Kapitein. 2017. Differentiation between Oppositely Oriented Microtubules Controls Polarized Neuronal Transport. *Neuron*. 96:1264-1271.

Trinczek, B., A. Ebneth, E.M. Mandelkow, and E. Mandelkow. 1999. Tau regulates the attachment/detachment but not the speed of motors in microtubule-dependent transport of single vesicles and organelles. *J Cell Sci*. 112 (Pt 14):2355-2367.

van Riel, W.E., A. Rai, S. Bianchi, E.A. Katrukha, Q. Liu, A.J. Heck, C.C. Hoogenraad, M.O. Steinmetz, L.C. Kapitein, and A. Akhmanova. 2017. Kinesin-4 KIF21B is a potent microtubule pausing factor. *Elife*. 6.

van Spronsen, M., M. Mikhaylova, J. Lipka, M.A. Schlager, D.J. van den Heuvel, M. Kuijpers, P.S. Wulf, N. Keijzer, J. Demmers, L.C. Kapitein, D. Jaarsma, H.C. Gerritsen, A. Akhmanova, and C.C. Hoogenraad. 2013. TRAK/Milton motor-adaptor proteins steer mitochondrial trafficking to axons and dendrites. *Neuron*. 77:485-502.

Verhey, K.J., and J.W. Hammond. 2009. Traffic control: regulation of kinesin motors. *Nat Rev Mol Cell Biol*. 10:765-777.

Verhey, K.J., N. Kaul, and V. Soppina. 2011. Kinesin assembly and movement in cells. *Annu Rev Biophys*. 40:267-288.

Vershinin, M., B.C. Carter, D.S. Razafsky, S.J. King, and S.P. Gross. 2007. Multiple-motor based transport and its regulation by Tau. *Proc Natl Acad Sci U S A*. 104:87-92.

Xu, J., B.J. Reddy, P. Anand, Z. Shu, S. Cermelli, M.K. Mattson, S.K. Tripathy, M.T. Hoss, N.S. James, S.J. King, L. Huang, L. Bardwell, and S.P. Gross. 2012. Casein kinase 2 reverses tail-independent inactivation of kinesin-1. *Nat Commun*. 3:754.

Yadav, S., P.J. Verma, and D. Panda. 2014. C-terminal region of MAP7 domain containing protein 3 (MAP7D3) promotes microtubule polymerization by binding at the C-terminal tail of tubulin. *PLoS One*. 9:e99539.

Abbreviations

Ct – C-terminus

MAP – microtubule-associated protein

MT – microtubule

Nt – N-terminus

Figure Legends

Figure 1 – MAP7 family proteins are redundant in kinesin-1 dependent mitochondria transport

(A) Scheme of all MAP7 family proteins and KIF5B constructs used in this study. For MAP7 proteins, the conserved MT binding site (yellow) and kinesin-1-binding domain (orange) are indicated. For KIF5B, the motor domain (purple) and coil/tail regions (green) are indicated. The MAP7-binding coil (coil 1) on KIF5B is indicated, KIF5B-560 is referred as K560 in all figures.
(B) Streptavidin pull down assay with extracts of HEK293T cells over-expressing BirA, K560-GFP (bait) and the indicated Bio-mCherry-labeled proteins (prey) or a mCherry empty vector as a negative control analysed by Western blot. The red line indicates the position of mCherry and MAP7 family proteins.
(C) Immunostaining of control HeLa cells for all endogenous MAP7 family members and α-tubulin imaged on a widefield microscope. Zooms of the red boxed areas are shown as an insert in each image, whereas the corresponding merge is shown on the right.
(D - F) Western blot analysis of indicated HeLa knockout cell lines and siRNA-mediated knockdown experiments with indicated antibodies, Ku80 was used as a loading control for all experiments.
(G, I) Immunostaining of indicated HeLa cell conditions with a cytochrome c antibody. Cell outlines are indicated with grey dashed lines and zooms of the red boxed areas are shown below.
(H, J) Mitochondria distribution was scored per condition using cytochrome c staining, (H) n = 345 (wild type (WT)), n = 347 (KIF5B knockout (KO)), n = 332 (MAP7 KO), n = 338 (MAP7D1 knockdown (KD)) and n = 373 cells (MAP7D3 KO), from three independent experiments. WT vs KIF5B KO, P = 0.0002, Student's t test. All other conditions were not significantly different from WT (Student's t test), (J) n = 444 (WT + siLuciferase), n = 589 (MAP7 KO + siD1/D3) and for rescue conditions on top of MAP7 KO + siD1/D3: n = 261 (MAP7-FL), n = 277 (MAP7D1-FL), n = 324 (MAP7D3-FL), n = 297 (MAP7-Nt), n = 277 (MAP7D1-Nt), n = 296 (MAP7D3-Nt), n = 263 (MAP7-Ct), n = 267 (MAP7D1-Ct) and n = 416 (MAP7D3-Ct), all from three or four independent experiments . *, P <0.05. **, P <0.01, *** P <0.001, Student's t test.

Figure 2 – Kinesin-1 recruitment on MTs depends on MAP7 family proteins

(A) Widefield images of overexpressed K560-GFP construct in indicated HeLa control, knockout or knockdown conditions.

(B) Quantification of kinesin localization in HeLa cells. n = 234 (WT), n = 252 (MAP7 KO), n = 174 (MAP7D1 KD) and n = 254 cells (MAP7D3 KO), from three independent experiments. WT vs MAP7D3 KO, P = 0.0035 (Student's t test), all other conditions were not significantly different from WT (Student's t test).

(C) Widefield images of overexpressed K560-GFP in control or MAP7 triple knockout/knockdown (KO/KD) HeLa cells. Cells were co-stained with an α -tubulin antibody and DAPI. Zooms of the red boxed areas in the GFP-channels are shown in the second panel row. A schematic representative drawing of K560-GFP localization of each condition is shown at the bottom panel row.

(D) Widefield images of overexpressed K560-GFP and mCherry-tagged MAP7 rescue constructs in MAP7 triple KO/KD HeLa cells. A schematic representative drawing of K560-GFP localization of each condition is shown at the bottom panel row.

(E) Quantification of K560-GFP localization per condition categorized as: diffuse, along MTs or at corner MTs in the cell periphery. n = 459 (WT + siLuciferase), n = 485 (MAP7 KO + siD1/D3) and for rescue conditions on top of MAP7 KO + siD1/D3: n = 113 (MAP7-FL), n = 237 (MAP7D1-FL), n = 90 (MAP7D2-FL), n = 167 (MAP7D3-FL), n = 210 (MAP7-Nt), n = 186 (MAP7D1-Nt), n = 133 (MAP7D3-Nt), n = 176 (MAP7-Ct), n = 197 (MAP7D1-Ct) and n = 193 (MAP7D3-Ct) collected from two to four independent experiments.

(F) Quantification of MAP rescue construct localization in the presence of K560-GFP in MAP7 triple KO/KD condition from the same experiment as panel D and E. n numbers are the same as numbers in panel E.

Figure 3 – Kinesin-1 can redistribute its own activator MAP7D3 in cells

(A) Widefield images of overexpressed K560-GFP construct in WT HeLa cells co-stained with antibodies against endogenous MAP7 or MAP7D3 and DAPI.

(B) Quantification of MAP7 and MAP7D3 localization at cell corner MTs in K560-GFP transfected HeLa cells as in A. n = 232 (MAP7) and n = 303 (MAP7D3) from three independent experiments, P = < 0.0001, Student's t test.

(C) Schematic drawing of the blue light-inducible optogenetic K560-LEXY motor containing a c-myc NLS N-terminal and a SV40 Large T-antigen NLS C-terminal of the mCherry tag. Blue light induces a conformation change, exposing the Jα-peptide containing a nuclear export signal from the LOV2 domain.

(D, G) Single frames of KIF5B KO cells double transfected with K560-LEXY and GFP-MAP7 (D) or GFP-MAP7D3 (G) sequentially illuminated with green and blue light sources (in that specific order) over the course of 4 minutes. Enlargements indicated with a yellow rectangle are shown below all single frame images. Acquisition was performed at one frame per five seconds.

(E, F, H, I) Measurements of fluorescence intensity changes over time in K560-LEXY positive cell corners. Each black line represents a single measurement of K560-LEXY (E,H),GFP-MAP7 (F) and GFP-MAP7D3 (I). n = 31 measurements from 17 cells (E, F) and n = 22 measurements from 14 cells (H, I), all from two independent experiments.

(J) Single frames of FRAP experiments on COS7 cells transiently transfected with GFP-MAP7 or GFP-MAP7D3. The images show the cell during baseline period (pre-FRAP), just after photobleaching (T = 0) of a 10x10 μm square region indicated with a red box, and at the indicated timepoints after photobleaching.

(K) Quantification of fluorescence recovery of indicated GFP-tagged proteins after photobleaching. Graph shows mean curve (bold line) +/- SD curve (light colored lines) over time. N = 18 cells (GFP-MAP7) and n = 18 cells (GFP-MAP7D3) from three independent experiments.

Figure 4 – Density and mobility of MAPs are determinant for kinesin-1 landing and processivity

(A) Representative kymograph of SNAP(Alexa647)-MAP7 or MAP7D3 diluted to single molecule levels on dynamic MTs in vitro. Movies were acquired at 25 frames/sec on a TIRF microscope.

(B) Quantification of labeling intensities of increasing concentrations of MAP7 and MAP7D3 on dynamic MTs using images obtained under identical laser power and exposure time on a TIRF microscope. n = 41 (MAP7, 2 nM), n = 44 (MAP7, 5 nM), n = 49 (MAP7, 20 nM), n = 39 (MAP7D3, 2 nM), n = 42 (MAP7D3, 5 nM) and n = 40 (MAP7D3, 20 nM) MTs from two independent experiments. Representative images are found in Fig S3A.

(C) Quantification of kinesin landing frequencies per MT and corrected for MT length, time of acquisition and kinesin concentration. n = 167 (control), n = 15 (MAP7, 2 nM), n = 14 (MAP7, 5 nM), n = 12 (MAP7, 20 nM), n = 13 (MAP7D3, 2nM), n = 15 (MAP7D3, 5 nM) and n = 25 MTs (MAP7D3, 20 nM) from two independent experiments.

(D) Representative kymographs of K560-GFP on dynamic MTs in control conditions or in the presence of increasing concentrations of MAP7 or MAP7D3.

(E) Quantification of all individual K560-GFP run length. *, P <0.05. **, P <0.01, *** P <0.001, Mann-Whitney U test. n = 241 (control), n = 351 (MAP7, 2 nM), n = 614 (MAP7, 5 nM), n = 361 (MAP7, 20 nM), n =257 (MAP7D3, 2nM), n = 436 (MAP7D3, 5 nM) and n = 303 (MAP7D3, 20 nM) from two independent experiments.

(F and G) Cumulative distributions of K560-GFP run length measured in presence of increasing concentrations of MAP7 (F) or MAP7D3 (G). Straight dashed lines correspond to single exponential fits, n numbers correspond to panel E.

(H) Gaussian distributions of kinesin velocities under indicated conditions. Frequency histograms of these velocities are found in fig S3B.

(I) Representative kymographs of dual-color in vitro reconstitution experiments with K560-GFP and SNAP(Alexa647)-tagged MAP7 or MAP7D3.

(J) Quantification of kinesin tracks positive for MAP7 or MAP7D3 co-transport, n = 417 (MAP7) and n = 344 (MAP7D3) from two independent experiments, *** P <0.001, Mann-Whitney U test.

Figure 5 – Addition of a weak MT-binding module is sufficient to make kinesin-1 processive

(A) Representative kymograph of K560-GFP on dynamic MTs in the presence of MAP7D3 full-length or Ct (both purified from *E.coli*), acquired on a TIRF microscope.

(B) Quantifications of MT labeling intensities of MAP7D3 full-length or Ct on dynamic MTs using images obtained under identical laser power and exposure time on a TIRF microscope. n = 40, n= 38 and n= 42 MTs from two independent experiments. Representative images are found in Fig S4A.

(C) Quantification of landing frequency per MT and corrected for MT length, time of acquisition and kinesin concentration. n = 167 (control), n = 36 (MAP7D3-FL, 20 nM), n = 36 (MAP7D3-Ct, 20 nM) and n= 31 (MAP7D3-Ct, 75 nM) from two independent experiments.

(D) Quantification of K560-GFP run length. *** P <0.001, Mann-Whitney U test. (D and E) n = 241 (control), n = 271 (MAP7D3-FL, 20 nM) and n = 209 (MAP7D3-Ct, 20 nM).

(E) Gaussian distributions of kinesin velocities under indicated conditions. Histograms of the velocities for each condition are found in Fig S4B.

(F) Kymographs of single molecule FRAP experiments on K560-GFP motors and MAP7D3-Ct imaged on a TIRF microscope. High intensity photobleaching with a 561 red laser was done at timepoints indicated with a red lightning bolt. Fluorescent recovery is indicated with a yellow arrow.

(G) Cumulative frequency distribution plot of mCherry-MAP7D3-Ct recovery after photobleaching (black dots) fitted to a one phase exponential decay (red line) with indicated decay constant (tau), n = 79 from three independent experiments.

Figure 6 – The MAP7 C-terminus can activate kinesin-1

(A) Coomassie blue-stained SDS Page showing a MT pelleting assay to study MT binding behavior of mCherry-MAP7-Ct. S: supernatant and P: pellet. Uncropped gel images are found in Fig S4C

(B) Representative kymographs of a dual-chamber in vitro experiment where equal concentrations of 10 nM K560-GFP motors where added to chambers with or without MAP7-Ct$_{(mini)}$. The experiment was performed on dynamic MTs and imaging was done by alternating acquisitions of both chambers on the same slide on a TIRF microscope.

(C) Kinesin landing frequencies quantified per MT and corrected for MT length, time of acquisition and kinesin concentration. Each independent dual-chamber experiments is color-coded, n = 32 (control) and n = 29 (MAP7-Ct$_{(mini)}$) from three independent experiments, P = <0.0001, Student's t-test.

(D) Histograms of K560-GFP velocities in the absence and presence of MAP7-Ct$_{(mini)}$. Red lines show fitting with Gaussian distribution, n = 404 (control) n = 648 measurements (MAP7-Ct$_{(mini)}$) from three independent experiments.

(E) Comparison of K560-GFP velocities described in D, colored lines show Gaussian fittings.

(F) Quantification of K560-GFP run length in the absence and presence of MAP7-Ct(mini). P = 0.008, Mann-Whitney U test, n = 404 (control) and n = 648 measurements (MAP7-Ct(mini)) from three independent experiments.

Figure 7 – Removal of the kinesin-1 stalk domain enhances motor landings

(A) Schematic overview of kinesin-1 truncation constructs.

(B) Coomassie blue-stained SDS Page gel showing purified K370-GFP and K560-GFP proteins used in this study. Protein quantities were determined using BSA standards and compared from a single gel.

(C) Representative kymographs of K370-GFP and K560-GFP motors walking on dynamic MTs.

(D) Quantification of kinesin landing frequencies, n = 57 (K370-GFP) from three independent experiments and n = 167 (K560-GFP) from two independent experiments, P = <0.0001, Mann-Whitney U test.

(E) Summarizing table of the characteristics and effects of MAP7 proteins on different parameters of kinesin activity observed in vitro and in cells.

(F) A model of kinesin-1 activation by MAP7 family proteins. KIF5B-560 can exist in different conformations that are less or more favorable for MT binding. MAP7 stabilizes the latter one, promoting motor landing on MTs. Subsequently, the kinesin rapidly dissociates from MAP7 but can “hop on” to the next MAP7 molecule present on the MT. MAP7-Ct can promote the landing of KIF5B-560 motors to which it is bound, but has no positive effect on processivity likely due to its rapid dissociation.

Supplemental Figure Legends

Figure S1 – Kinesin-1 recruitment to MTs by MAP7 family C-termini

(A) Widefield images of overexpressed GFP-MAP7D3-Ct rescue construct in MAP7 triple KO/KD HeLa cells stained with red MitoTracker and DAPI to visualize mitochondria and nuclei.
(B) Widefield images of overexpressed constructs K560-GFP with mCherry-tagged rescue constructs Nt and Ct in MAP7 triple KO/KD HeLa cells. Enlargements of images indicated with a red squared box are in the panel row below. A schematic and representative drawing of K560-GFP localization over each condition is shown at the bottom panel row.

Figure S2 – Overview and analysis of purified proteins

(A) Coomassie blue-stained SDS gels showing the purified proteins used in this study.
(B) Results of Mass-Spectrometry analysis of purified K560-GFP motors washed with normal (0.3 M) or high-salt (1.5 M NaCl).
(C) Western blot analysis of purified K560-GFP motors washed with normal (0.3 M) or high-salt (1.5 M NaCl). Antibodies against GFP, MAP7 and MAP7D3 were used, GFP serves as a loading control.

Figure S3 – MT binding of MAP7/MAP7D3 and its effects on kinesin-1

(A) Images showing increasing concentrations of SNAP(Alexa647)-tagged MAP7 or MAP7D3 on in vitro reconstituted dynamic MTs. Images were obtained under identical laser power and exposure time on a TIRF microscope. Right images show replicate images from the left with linearly increased brightness/contrast (ImageJ software).
(B) Histograms of K560-GFP velocities in control conditions or in presence of indicated proteins. Red lines show fitting with Gaussian distributions, mean values with standard deviation are indicated in the plot, n = 241 (control), n = 351 (MAP7, 2 nM), n = 614 (MAP7, 5 nM), n = 361

(MAP7, 20 nM), n =257 (MAP7D3, 2nM), n = 436 (MAP7D3, 5 nM) and n = 303 (MAP7D3, 20 nM) from two independent experiments.

(C) Histograms of fluorescence intensities of single GFP molecules (immobilized on coverslips) and K560-GFP moving on MTs with or without mCherry-MAP7D3-FL (purified from *E.coli*) in two separate chambers on the same coverslip (dots) and the corresponding fits with lognormal distributions (lines). n = 858 (GFP), n = 1640 (K560-GFP) and n = 4137 molecules (K560-GFP + mCherry-MAP7D3-FL); fluorophore density was approximately 0.01 μm^{-2} for GFP and K560-GFP proteins were analyzed from 2-10 MTs per movie. Dashed lines show corresponding relative median values.

(D) Representative kymographs of 1:1 mixed K560-GFP (green) and K560-SNAP(Alexa647) (magenta) moving on dynamic MTs with or without mCherry-MAP7D3-FL (purified from *E.coli*). Maximum intensity projections show rhodamine-labeled MTs (control) or mCherry-MAP7D3-FL labeled MTs in red.

Figure S4 – Analysis of kinesin properties and MT binding of MAP truncations

(A) Images showing increasing concentration of mCherry-tagged MAP7D3 full-length or Ct (purified from *E.coli*) on in vitro reconstituted dynamic MTs. Images were obtained under identical laser power and exposure time on a TIRF microscope. Right images show replicate images from the left with linearly increased brightness/contrast (ImageJ software).

(B) Histograms of K560-GFP velocities in control conditions or in presence of indicated proteins. Red lines show fitting with Gaussian distributions, mean values with standard deviation are indicated in the plot, n = 271 (MAP7D3-FL) and n = 209 (MAP7D3-Ct)

(C) Unprocessed Coomassie blue-stained SDS Page gels of a MT pelleting assay shown in Fig 6A. Two SDS gels were loaded with quantitatively different inputs: 40 and 2.5% of total samples. Positions of tubulin and MAP7-Ct truncation on gel are indicated on the right.

(D) Images showing in vitro polymerized MTs, labeled with HiLyte 488 tubulin, with mCherry-MAP7-Ct. Images were obtained on a TIRF microscope. Rhodamine labeled GMPCPP MT seeds are indicated (red arrow). The mCherry-MAP7-Ct image is shown on the right with linear increased brightness/contrast (ImageJ software).

(E) Histograms showing K370-GFP and K560-GFP velocities and its Gaussian fits (red line). Mean values are indicated with their standard deviation in the respective plots. n = 723 (K370-GFP) and n = 329 (K560-GFP).

(F) Quantification of K370- and K560-GFP run length. P = 0.03, Mann-Whitney U test, n = 723 (K370) and n = 241 measurements (K560) from two independent experiments.

Supplemental Videos

Video 1 – Imaging of blue light-induced nuclear export of K560-LEXY with GFP-MAP7

Sequential dual-color acquired video of GFP-MAP7 (left) and K560-mCherry-LEXY (right) in KIF5B KO HeLa cells. The video was acquired at a 5 sec per frame over the course of 4 min time on a spinning disc confocal microscope setup. Video corresponds to Fig. 3D.

Video 2 – Imaging of blue light-induced nuclear export of K560-LEXY with GFP-MAP7D3

Sequential dual-color acquired video of GFP-MAP7D3 (left) and K560-mCherry-LEXY (right) in KIF5B KO HeLa cells. The video was acquired at a 5 sec per frame over the course of 4 min time on a spinning disc confocal microscope setup. Video corresponds to Fig. 3G.

Figure 1 - Hooikaas et al.

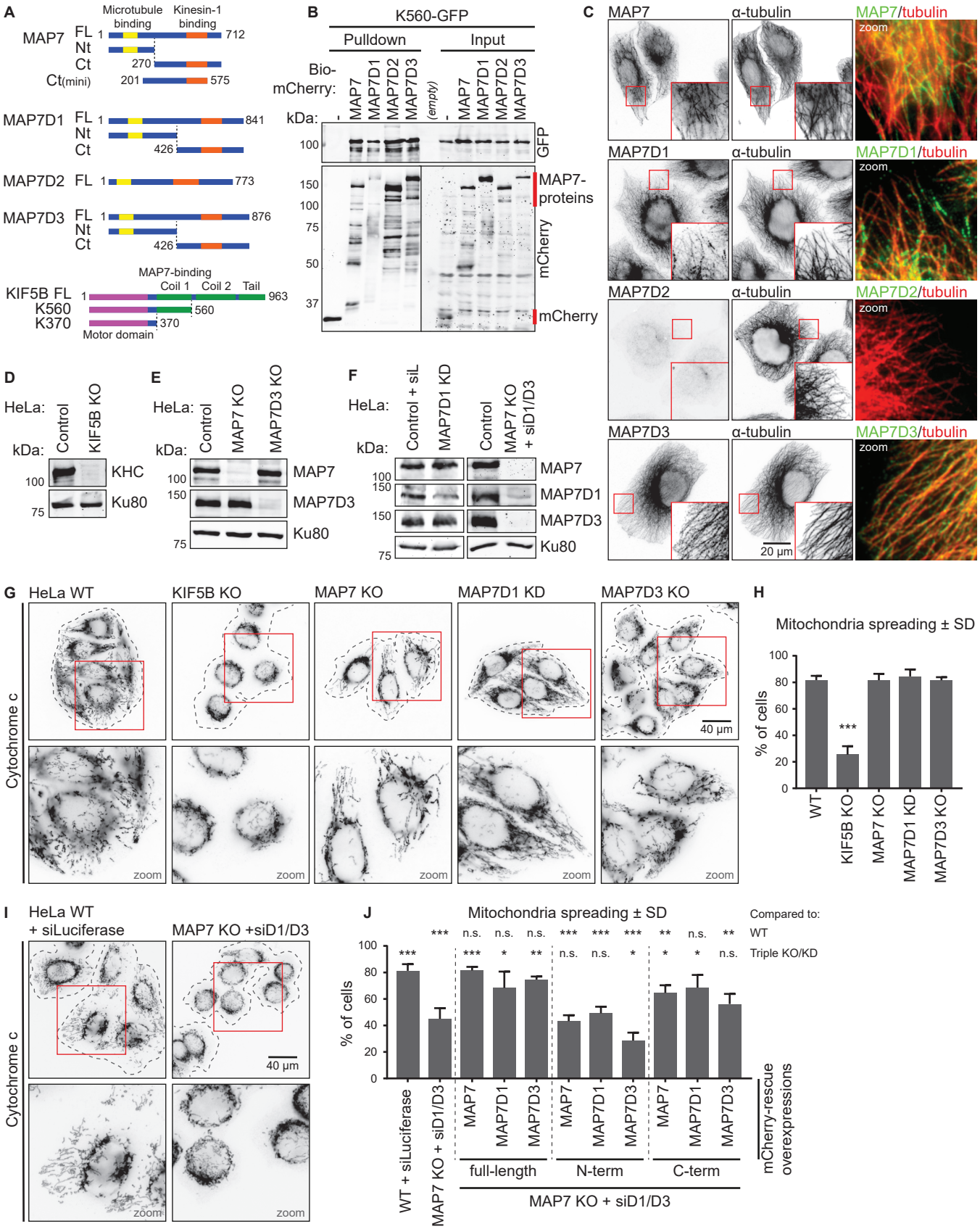

Figure 2 - Hooikaas et al.

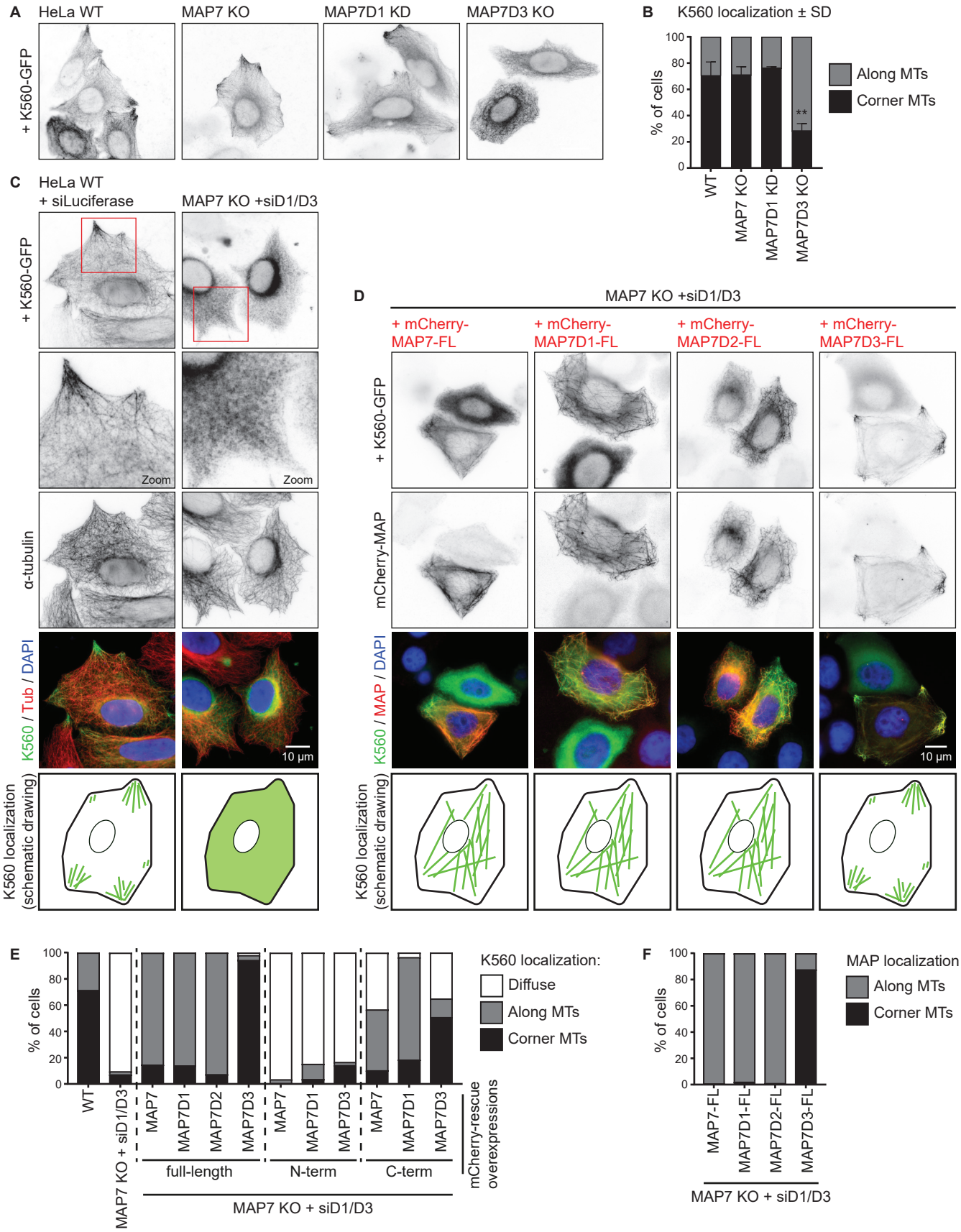

Figure 3 - Hooikaas et al.

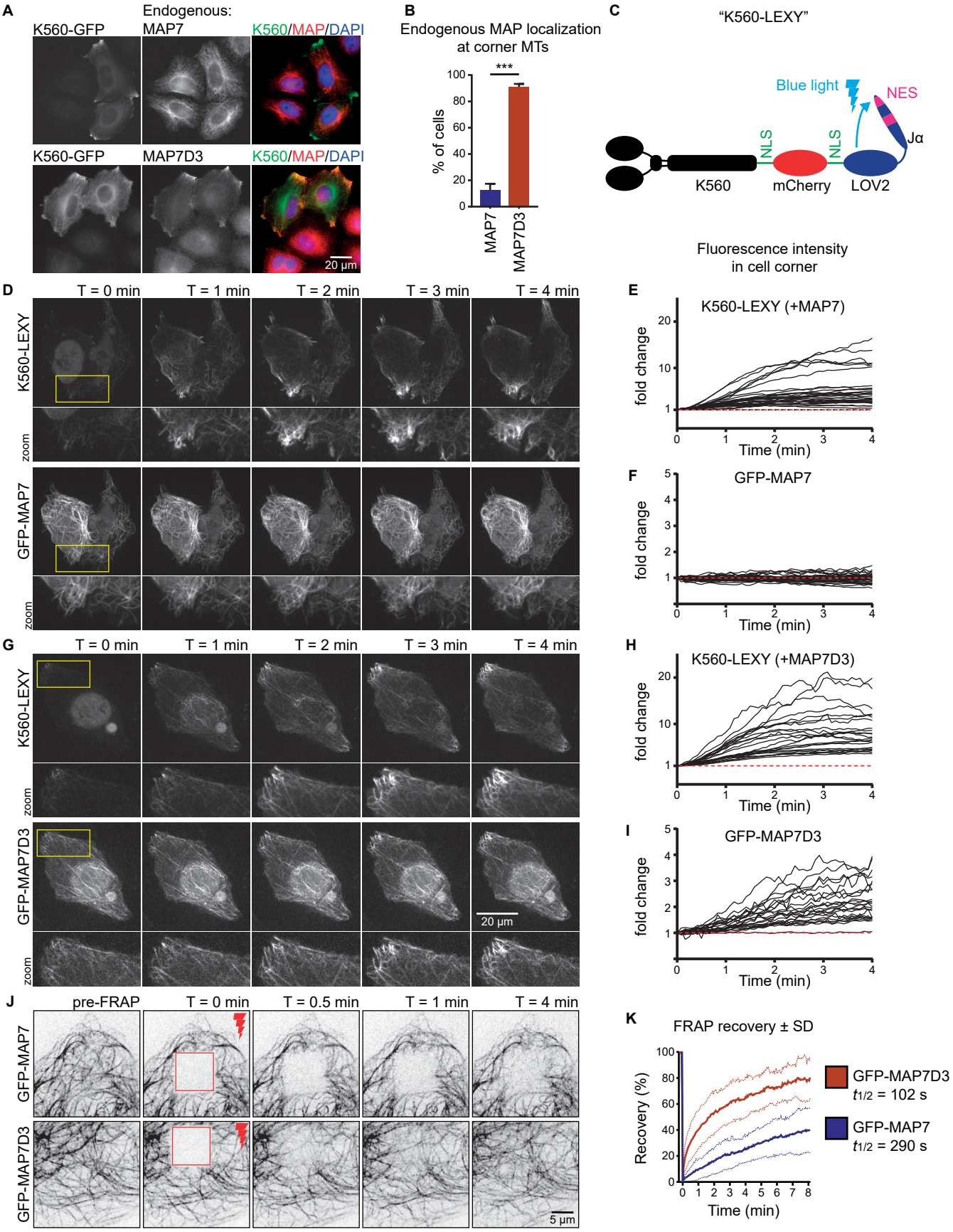

Figure 4 - Hooikaas et al.

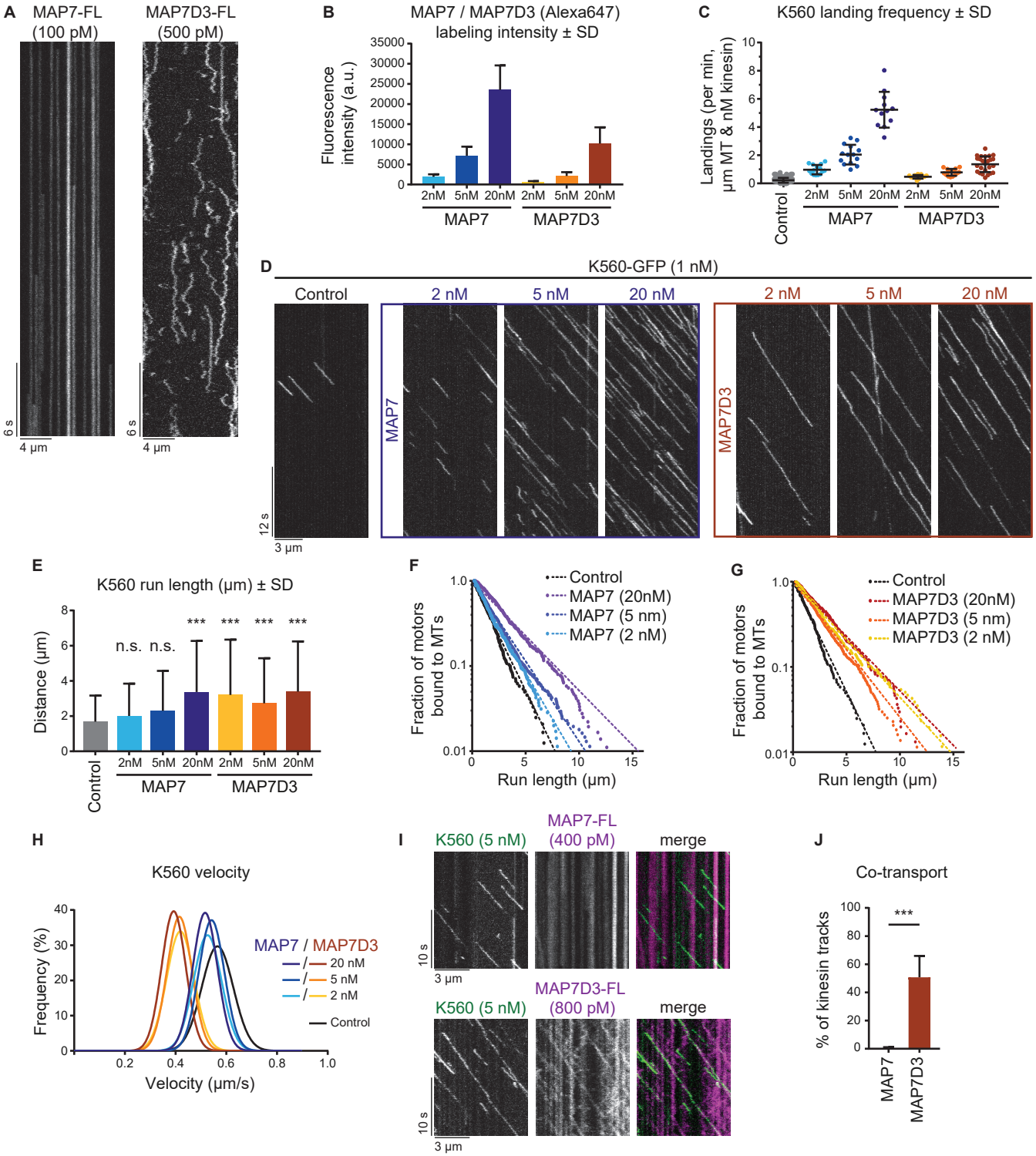

Figure 5 - Hooikaas et al.

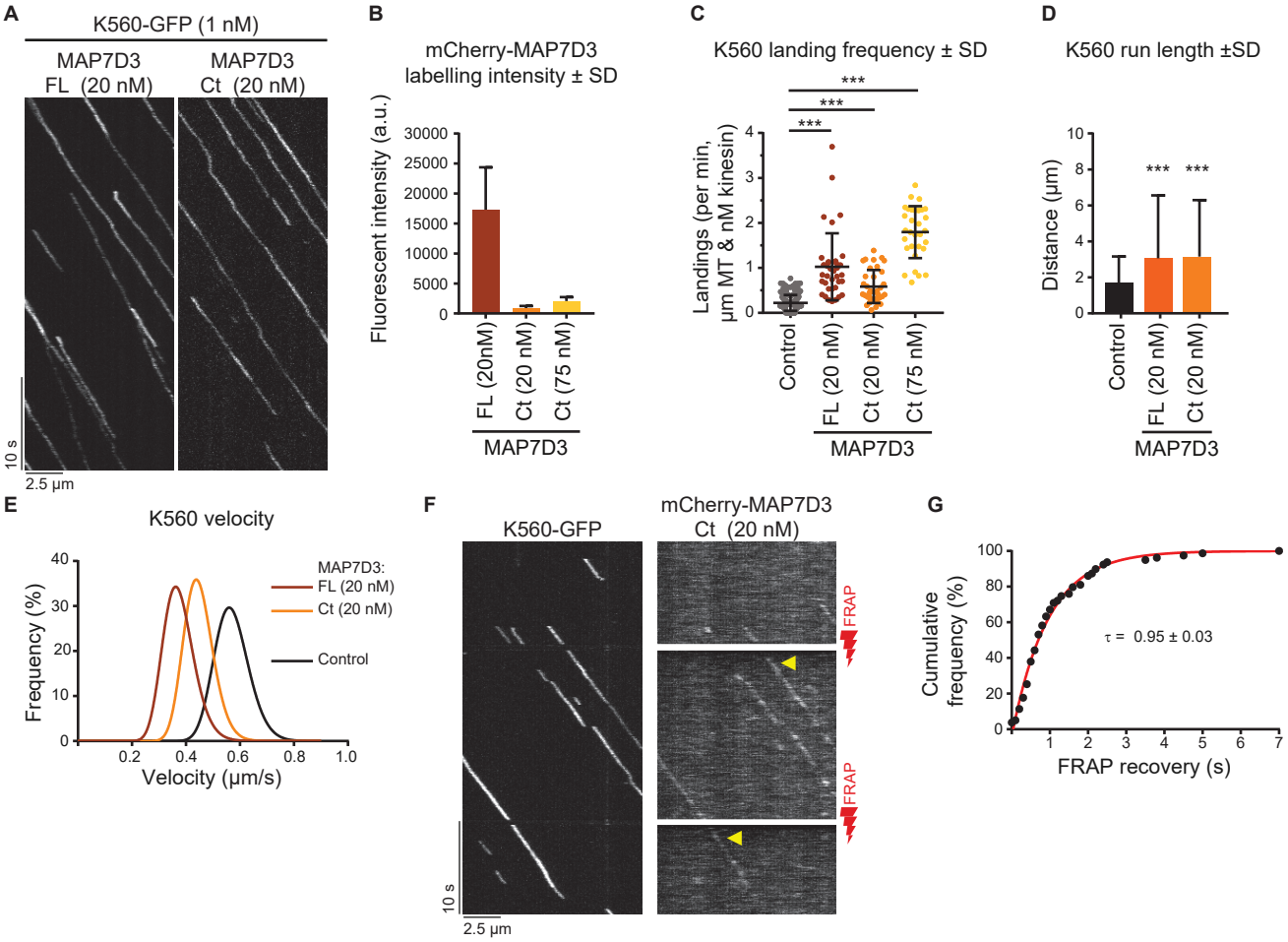

Figure 6 - Hooikaas et al.

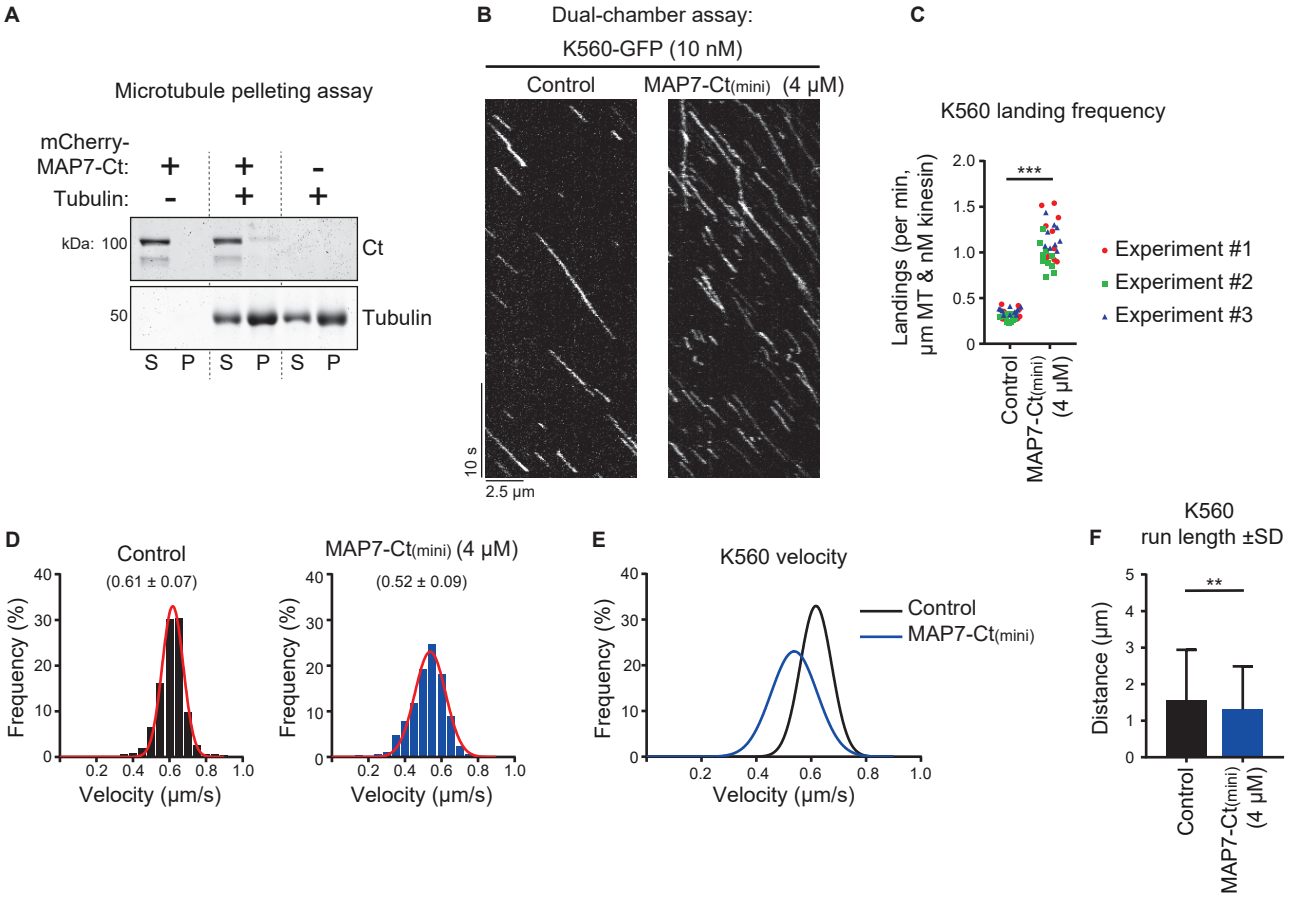

Figure 7 - Hooikaas et al.

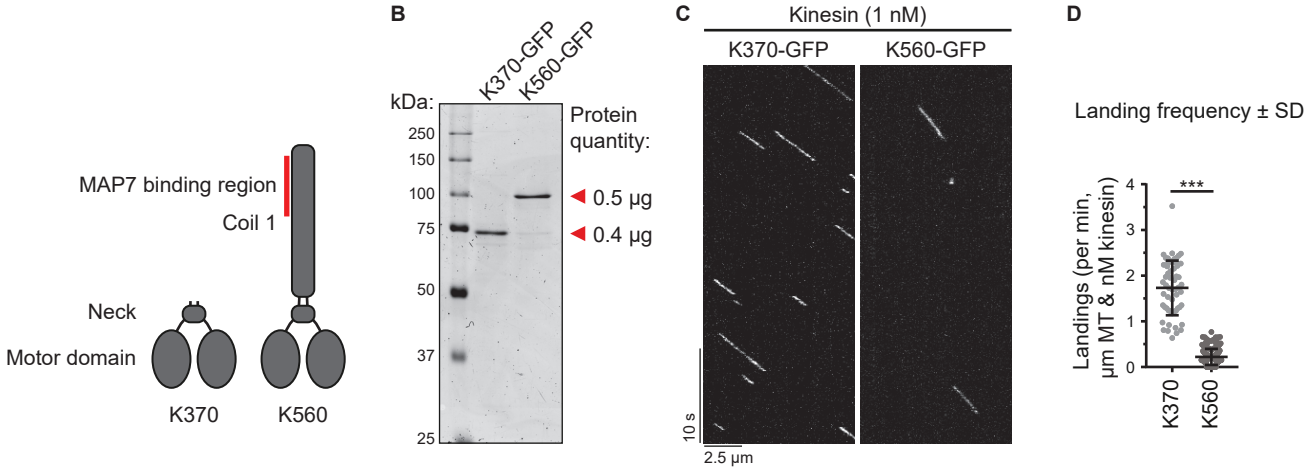

E

Construct		MT binding	K560 recruitment	K560 processivity	K560 velocitiy	Co-transport with K560	K560 recruitment	Redistribution by K560	Mitochondria spreading
MAP7	FL	+ + + +	+ + + +	↑↑	no effect	no effect	+ + +	no effect	+ + +
MAP7	Ct	no binding	+	-	↓	not analyzed	+ +	no effect	+ +
MAP7D3	FL	+ + +	+ + +	↑↑↑	↓↓↓	+ + +	+ + +	+ + +	+ + +
MAP7D3	Ct	+	+ +	↑↑↑	↓↓	+ +	+ +	+ +	+ +
		in vitro					in cells		

F

Model of kinesin-1 activation by MAP7 proteins

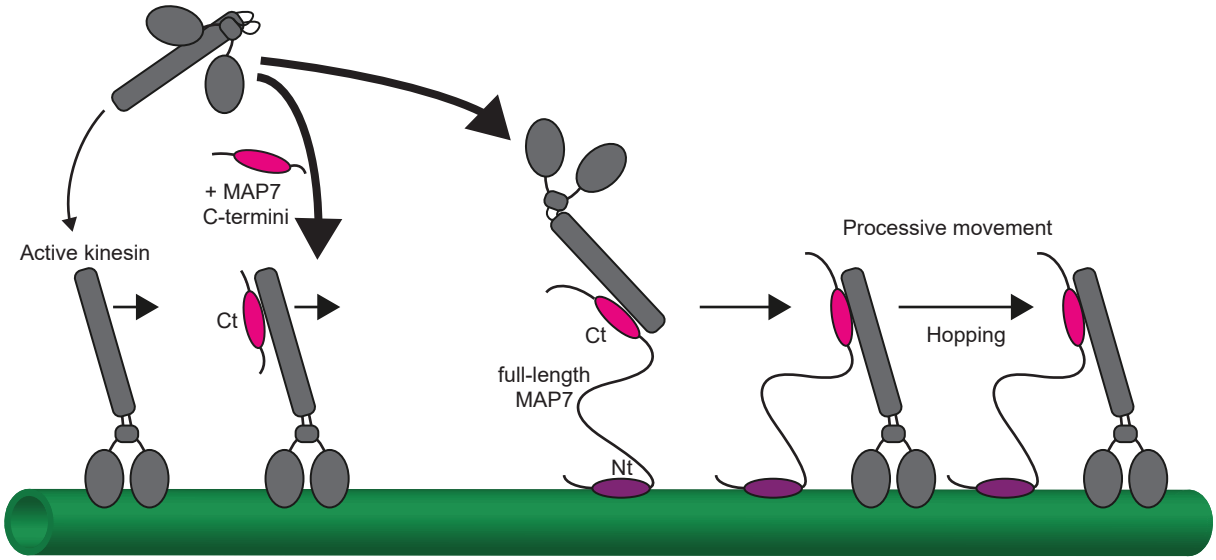

Figure S1 - Hooikaas et al.,

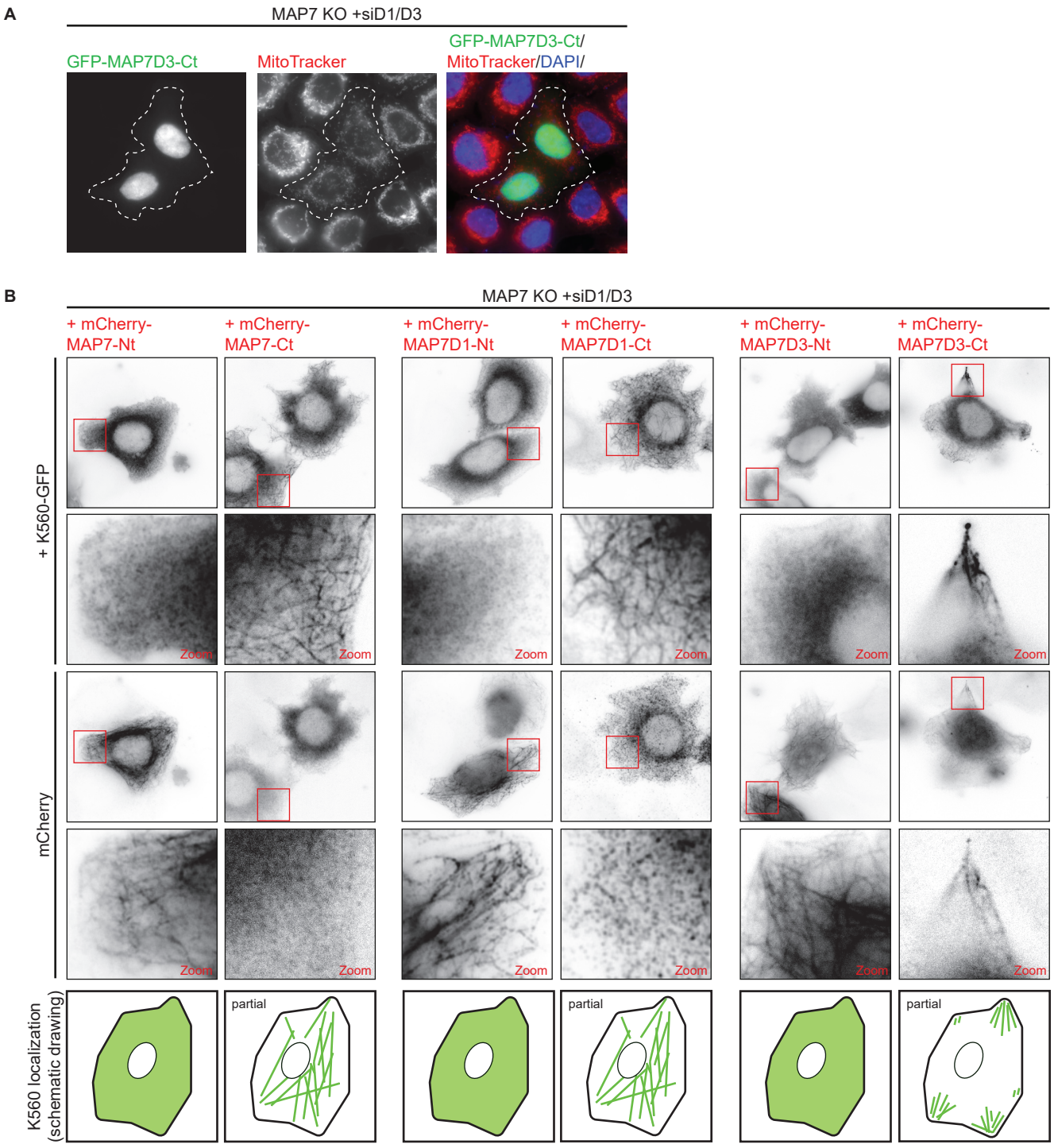

Figure S2 - Hooikaas et al.

A

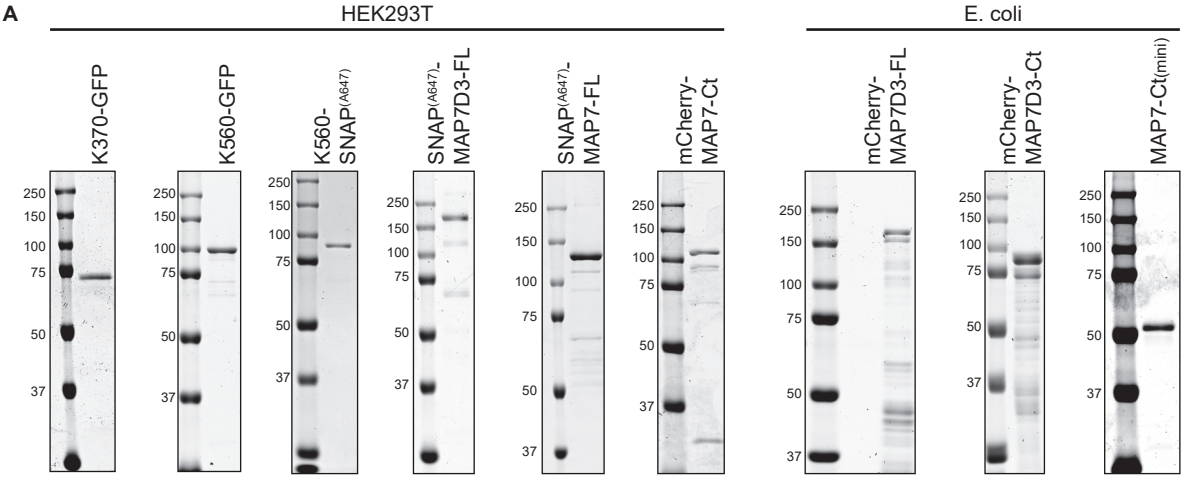

B

Low-Salt (0.3M) washed K560-GFP

Name	Score	Coverage (%)	Total Peptides
Kinesin-1 heavy chain (KIF5B)	59099.21	63.03	105
MAP7	174.13	10.12	5
MAP7D1	130.75	8.11	5
MAP7D3	162.35	3.12	2

High-Salt (1.5M) washed K560-GFP

Name	Score	Coverage (%)	Total Peptides
Kinesin-1 heavy chain (KIF5B)	54398.88	59.40	98
MAP7			
MAP7D1	0	1.03	1
MAP7D3			

C

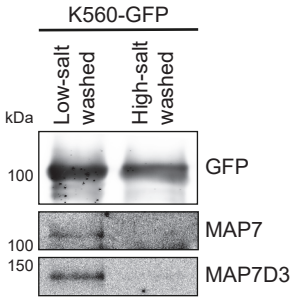

Figure S3 - Hooikaas et al.

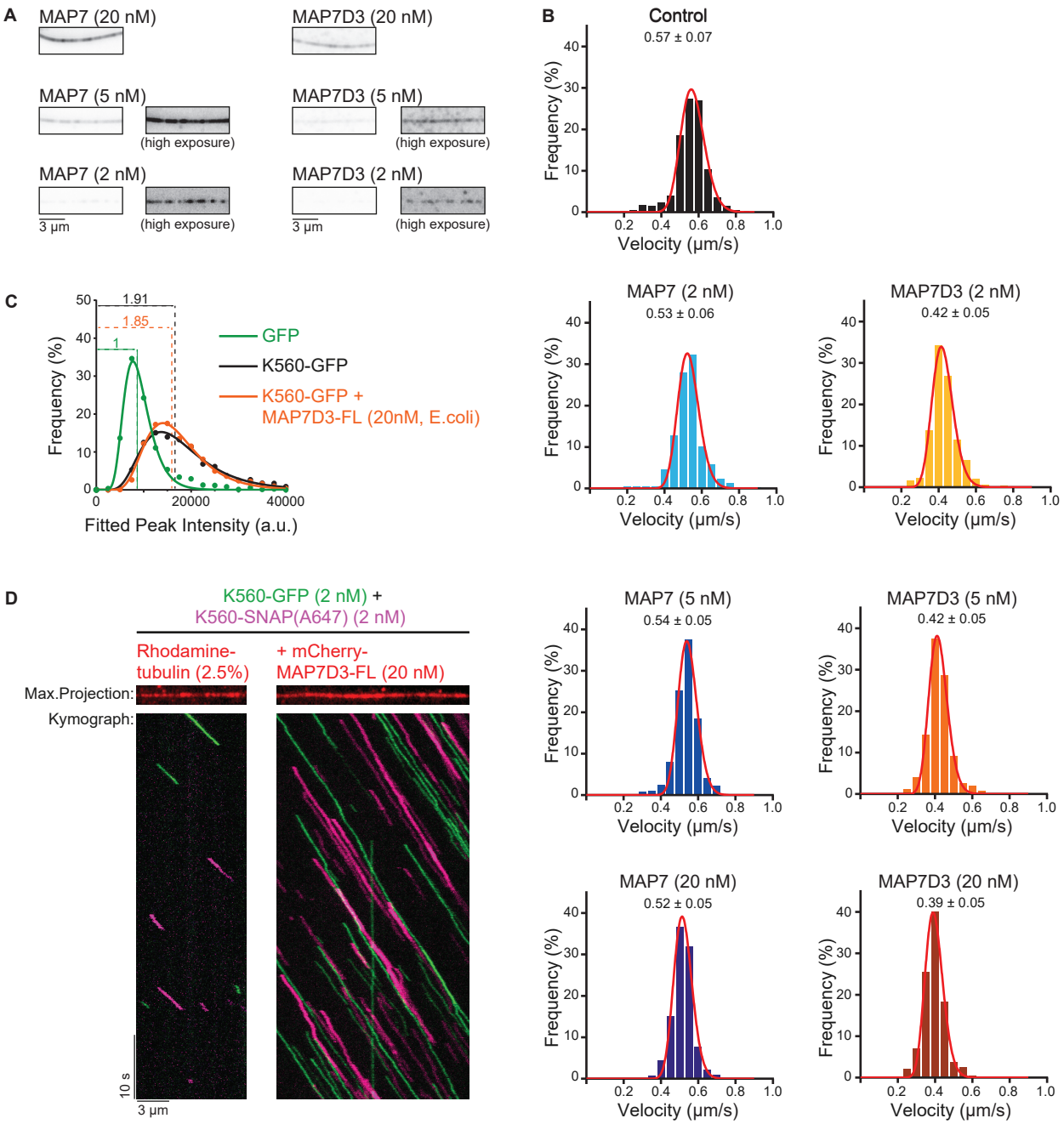
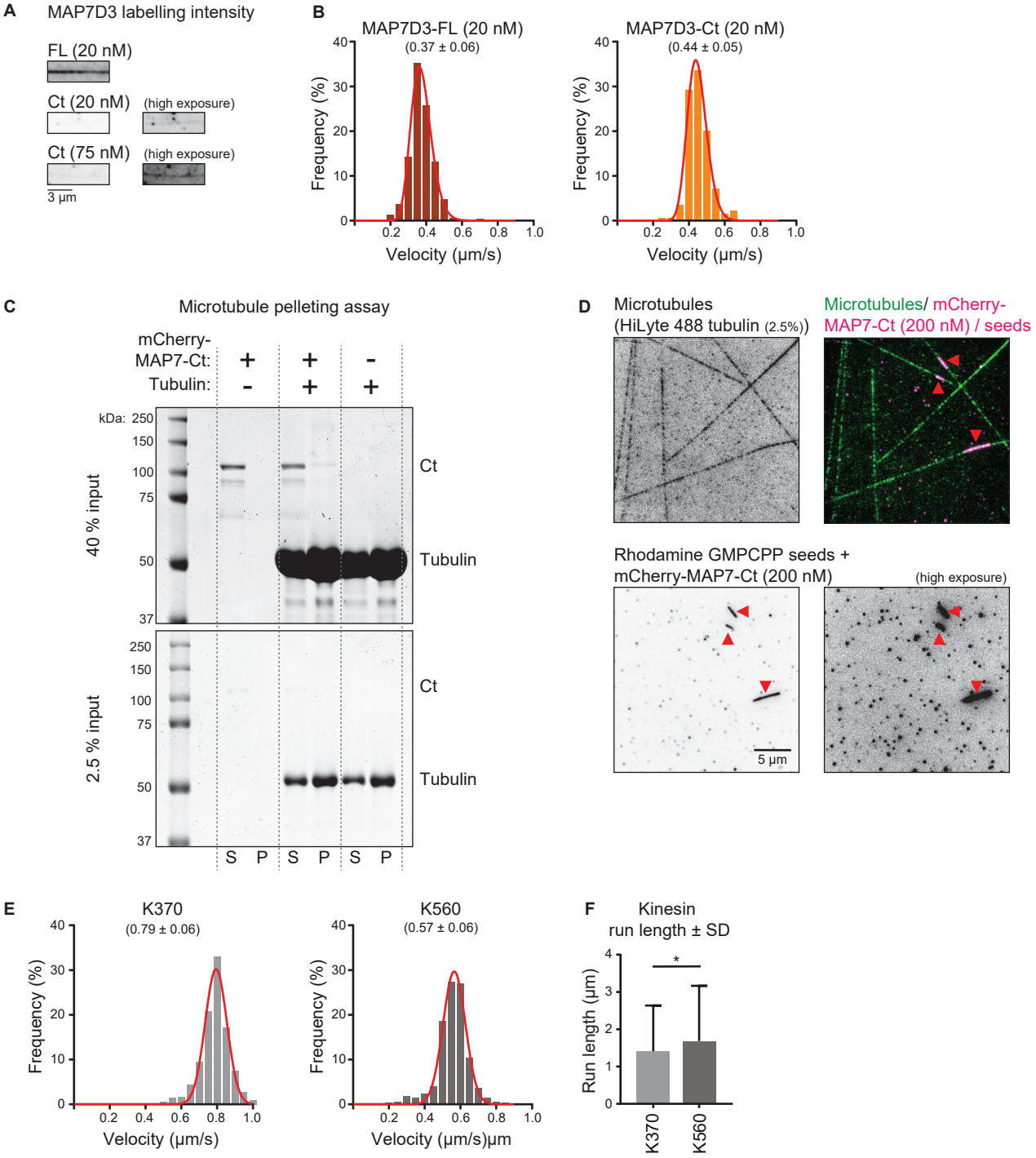
Figure S4 - Hooikaas et al.